(**Fig. 4f,g**), suggesting that increased insulin sensitivity observed in *Angptl6* transgenic mice depends on direct effects of increased serum AGF.

Resistance to obesity in *Angptl6*-transgenic mice

To investigate whether *Angptl6* transgenic mice show resistance against developing obesity, we challenged 8-week-old female mice with a high-fat diet containing 32% (wt/wt) fat for 12 weeks to stimulate weight gain. *Angptl6* transgenic mice fed this diet showed significant differences from controls: at the end of the feeding period, the net weight gains were 7.13 ± 1.03 g and 21.86 ± 4.03 g, respectively, for *Angptl6* transgenic and controls (**Fig. 5a,b**). As expected, high-fat feeding causes massive lipid accumulation in both visceral and subcutaneous fat depots in controls, whereas few of these changes are seen in *Angptl6* transgenic mice (**Fig. 5c,d**). Notably, the size of WAT from *Angptl6* transgenic mice was markedly smaller than that of WAT from controls (**Fig. 5e**). No appreciable fatty acid accumulation in BAT, liver and skeletal muscle was observed in *Angptl6* transgenic mice, whereas nontransgenic mice develop tissue steatosis (**Fig. 5e,f**). There was no significant difference in blood glucose levels between genotypes (**Fig. 5g**). But plasma insulin levels in *Angptl6* transgenic mice were much lower than those seen in controls (**Fig. 5g**). Whereas high-fat feeding increases serum cholesterol and FFA levels by twofold in controls, *Angptl6* transgenic mice showed a lipid profile closer to that of wild-type mice fed a standard chow diet (**Fig. 5g**).

AGF antagonizes obesity and insulin resistance

To clarify whether AGF decreases body weight and insulin resistance of obese mice, we intravenously injected adenovirus expressing mouse AGF (Ad-AGF) into female mice fed a high-fat diet containing 32% (wt/wt) fat for 12 months. For controls, adenovirus expressing green fluorescent protein (GFP) (Ad-GFP) was injected. There was no significant difference in body weight between the mice with AGF treatment and controls (54.4 ± 2.2 g and 52.9 ± 2.1 g, respectively: $P = 0.18$, $n = 8$). Throughout the time course of the experiment, mice continued to receive a high-fat diet. On day 20, mice receiving AGF showed approximately 2.5-fold increases in serum AGF levels compared to controls (**Fig. 6a**), and showed significant loss of body weight compared to controls (**Fig. 6b**). No significant difference between the two groups was observed in daily food intake (**Fig. 6c**). Furthermore, significant decreases in fasting and random fed glucose levels were observed in high-fat diet–induced obese mice after treatment with AGF compared to those in controls (**Fig. 6d,e**). IGTT and IITT showed that high-fat diet–induced obese mice with AGF treatment showed improved glucose tolerance and increased insulin sensitivity (**Fig. 6f,g**). Taken together, these data clearly show that AGF counteracts obesity and related insulin resistance.

DISCUSSION

AGF, a member of the Angptl family, is a circulating angiogenic protein secreted by liver[7]. Here, we show that most (>80%) of the AGF-deficient mice die at approximately embryonic day 13, with apparent cardiovascular defects including poorly formed yolk sac and vitelline vessels. Notably, the surviving *Angptl6*$^{-/-}$ mice become markedly obese and show obesity-related metabolic disorders. Furthermore, *Angptl6*$^{-/-}$ mice show decreased whole-body oxygen consumption and expression of genes involved in energy dissipation. In parallel, *Angptl6* transgenic mice show resistance against diet-induced obesity, insulin resistance and hyperlipidemia. These phenotypes are associated with increases in energy expenditure, supporting the hypothesis that AGF regulates energy metabolism in mice.

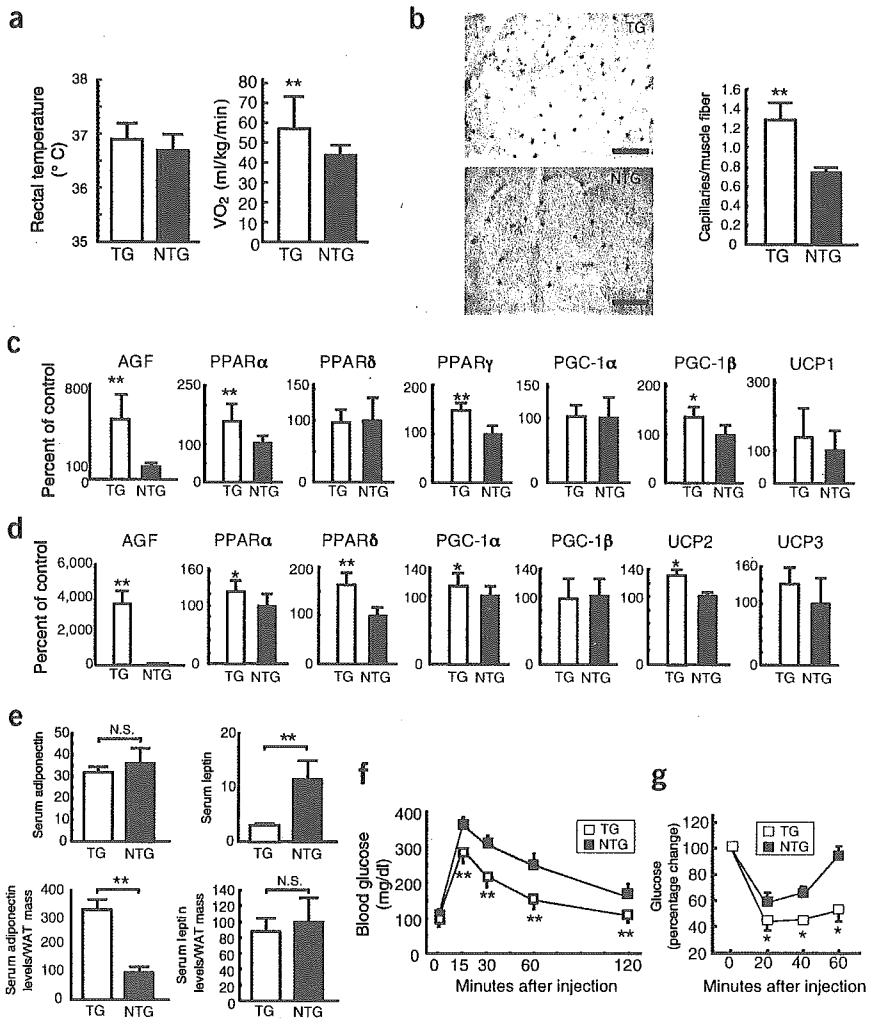

Figure 4 Metabolic and vascular alteration in *Angptl6* transgenic mice. (**a**) Rectal temperature and oxygen consumption (VO_2)/lean body weight in *Angptl6* transgenic (TG) and nontransgenic (NTG) female mice at 5 months of age (n = 10–12 in each group; these mice were also used in **Fig. 4e,f**). (**b**) Representative photograph of CD31/PECAM-1-stained capillary vessels and quantitative estimation of capillary vessel density in the gastrocnemius muscle in TG and NTG female mice at 4 months of age. Scale bars, 50 μm. (**c,d**) Relative ratio of gene expression associated with increased energy expenditure in BAT (**c**) and skeletal muscle (**d**) in TG mice relative to that seen in NTG female and male mice at 4 months of age. The ratio for the data from NTG mice is set as 100%. (**e**) Serum adiponectin and leptin levels and serum adiponectin and leptin levels/ WAT mass in TG and NTG female mice at 4 months of age. (**f,g**) Glucose (**f**) and insulin (**g**) tolerance tests in TG and NTG female mice at 4 months of age. Data are mean ± s.d. (n = 5–15). *P < 0.05, **P < 0.01, between the two genotypes indicated. N.S. indicates no significant difference compared with NTG mice.

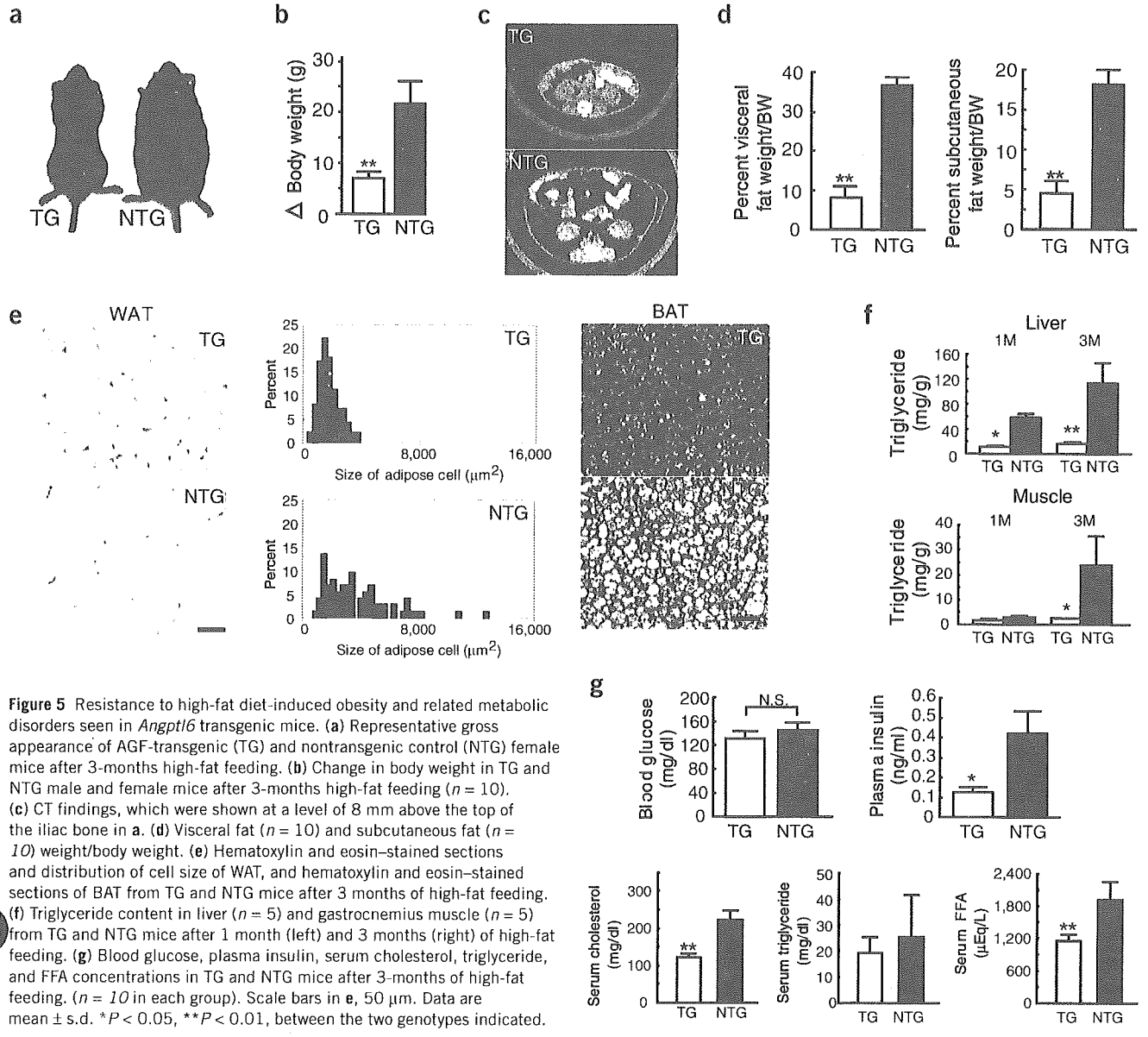

Figure 5 Resistance to high-fat diet-induced obesity and related metabolic disorders seen in *Angptl6* transgenic mice. (**a**) Representative gross appearance of AGF-transgenic (TG) and nontransgenic control (NTG) female mice after 3-months high-fat feeding. (**b**) Change in body weight in TG and NTG male and female mice after 3-months high-fat feeding ($n = 10$). (**c**) CT findings, which were shown at a level of 8 mm above the top of the iliac bone in **a**. (**d**) Visceral fat ($n = 10$) and subcutaneous fat ($n = 10$) weight/body weight. (**e**) Hematoxylin and eosin–stained sections and distribution of cell size of WAT, and hematoxylin and eosin–stained sections of BAT from TG and NTG mice after 3 months of high-fat feeding. (**f**) Triglyceride content in liver ($n = 5$) and gastrocnemius muscle ($n = 5$) from TG and NTG mice after 1 month (left) and 3 months (right) of high-fat feeding. (**g**) Blood glucose, plasma insulin, serum cholesterol, triglyceride, and FFA concentrations in TG and NTG mice after 3-months of high-fat feeding. ($n = 10$ in each group). Scale bars in **e**, 50 μm. Data are mean ± s.d. $^*P < 0.05$, $^{**}P < 0.01$, between the two genotypes indicated.

Metabolic analysis of energy balance using *Angptl6*$^{-/-}$ and *Angptl6* transgenic mice showed that one way AGF functions to regulate adiposity is through control of energy dissipation. Recent studies indicate that BAT and skeletal muscle regulate adaptive thermogenesis, which is mediated by PPARα, PPARδ, PPARγ and their coactivators, PGC-1α and PGC-1β, in response to energy overload[3,16,26,32–35]. We found statistically significant decreases in the expression of PPARα, PPARγ and PGC-1β in BAT and of PPARδ in skeletal muscle in *Angptl6*$^{-/-}$ mice, and increases in expression of PPARα, PPARγ and PGC-1β in BAT and of PPARα, PPARδ, and PGC-1α in skeletal muscle of *Angptl6* transgenic mice. In fact, *Angptl6* transgenic mice show phenotypes similar to those seen in transgenic mice with activated PPARδ[36–38] and PGC-1β[26]. Skeletal muscle is a direct target tissue of AGF, because AGF protein binds to C2C12 myocytes (**Supplementary Fig. 3** online). Treatment of C2C12 myocytes with AGF stimulated ligand activities of PPARα and PPARδ (**Supplementary Fig. 3**). Moreover, AGF activates p38 MAPK in muscle (**Supplementary Fig. 3**), which directly enhances the stabilization and activation of PGC-1 protein[34,35]. We therefore propose that AGF stimulates fat burning in peripheral tissues through the p38 MAPK pathway and downstream effects on respiration and gene expression linked to mitochondrial uncoupling and energy expenditure.

The microvasculature assists in heat dissipation at sites of active thermogenesis in peripheral tissues[28,29]. Because AGF increases the number of capillary-sized vessels in mice[8], we examined whether the vasculature is altered in *Angptl6*$^{-/-}$ and *Angptl6* transgenic mice. *Angptl6*$^{-/-}$ mice were susceptible to obesity and showed significantly ($P < 0.05$) decreased blood-flow perfusion in skeletal muscle, suggesting that loss of AGF enhances observed decreases in the efficiency in energy dissipation (**Supplementary Fig. 4** online). In parallel, a significant ($P < 0.01$) increase in the number of microvessels was observed in skeletal muscle of *Angptl6* transgenic mice, which may antagonize obesity by facilitat-

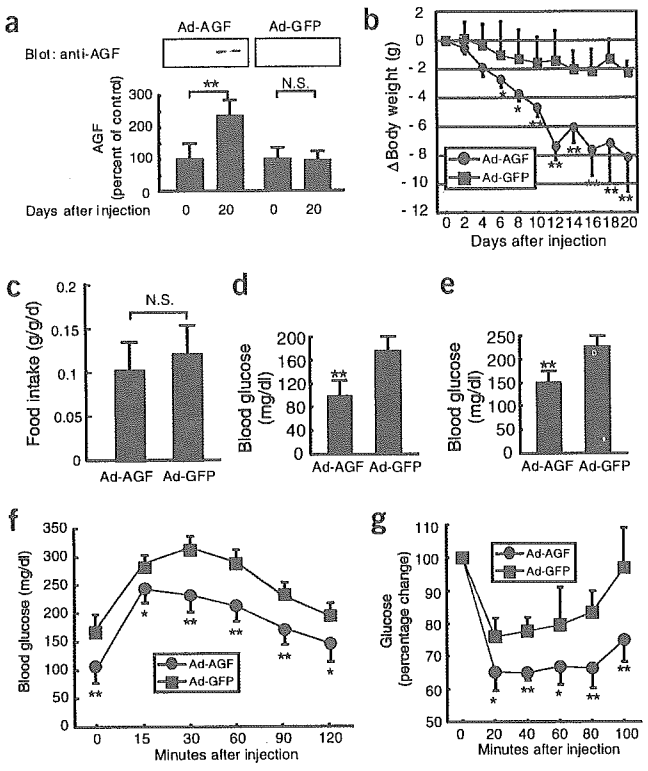

Figure 6 AGF decreased body weight and increased insulin sensitivity in high-fat fed-induced obese mice. (**a**) The relative ratio of serum concentrations of AGF in Ad-AGF injected and Ad-GFP injected mice on day 20 relative to each mouse on day 0. The value of serum AGF concentrations on day 0 is set at 100% ($n = 5$–8 in each group). (**b**) Alteration in body weight of high-fat fed-induced obese female mice after Ad-AGF and Ad-GFP injections ($n = 8$ in each group). (**c**-**g**) Comparison of food intake/lean body weight (**c**), fasting blood glucose (**d**), random fed blood glucose (**e**), glucose tolerance test (**f**) and insulin tolerance test (**g**) between Ad-AGF injected and Ad-GFP injected mice ($n = 5$-8 in each group). Data are mean ± s.d. $^*P < 0.05$, $^{**}P < 0.01$, between the two groups. N.S. indicates no significant difference compared with Ad-GFP–injected mice.

ing increases in energy dissipation. Furthermore, by providing a local angiogenic signal, AGF might increase the efficiency of lipid release from fat stores to maintain energy homeostasis. AGF induces angiogenesis in peripheral tissues, partially explaining how AGF counteracts obesity in addition to the direct effects of AGF on tissues functioning in adaptive thermogenesis.

Recent studies indicate that abnormal accumulation of triglycerides in muscle and liver results in insulin resistance by inhibiting insulin receptor signaling cascades[39,40]. Even on a high-fat diet, *Angptl6* transgenic mice are protected against hepatic and muscle steatosis, resulting in the maintenance of insulin sensitivity. These findings suggest that one mechanism whereby AGF affects insulin sensitivity is inhibition of abnormal lipid stores in insulin target tissues. Adipose tissue has a substantial impact on systemic glucose homeostasis through production of adipokines[34,35]. Recent studies show a role for adiponectin[20,21] and leptin[22,23] as mediators of insulin sensitivity and TNF-α[18,19] in mediating insulin resistance. In lipoatrophic diabetes, adiponectin and leptin deficiency resulting from lack of fat is associated with insulin resistance and diabetes[20,22,30,31]. Despite a greatly decreased WAT mass, *Angptl6* transgenic mice show increased insulin sensitivity, suggesting that AGF may increase insulin sensitivity. In contrast with decreased serum leptin levels, serum adiponectin levels in *Angptl6* transgenic mice were identical to those seen in wild-type mice. This may partially contribute to increased insulin sensitivity in *Angptl6* transgenic mice.

Findings derived from *Angptl6* transgenic mice, in which AGF expression is driven from the CAG promoter, led us to ask whether AGF in the circulation affects obesity and related metabolic abnormalities, because AGF is secreted primarily from hepatocytes. In this study, mice with high-fat diet–induced obesity overexpressing AGF in liver as a result of adenoviral transduction showed 2.5-fold increases in serum AGF levels over in controls and showed significant ($P < 0.01$) body weight loss and improved insulin sensitivity. Moreover, we observed that serum AGF levels in *Angptl6* transgenic mice described here and those seen in K14-*Angptl6* transgenic mice[7,8], in which AGF is driven by a skin-specific (K14) promoter, were approximately identical (**Supplementary Fig. 5** online). Notably, K14-*Angptl6* transgenic mice 8 months after birth show marked reduction in body weight and adiposity compared to controls, and this phenotype is similar to that seen in *Angptl6* transgenic mice created by driving *Angptl6* expression from the CAG promoter (**Supplementary Fig. 5**). K14-*Angptl6* transgenic mice also showed increased insulin sensitivity despite an extremely decreased WAT mass (**Supplementary Fig. 5**). These findings indicate that increasing serum AGF levels could counteract obesity and related insulin resistance, suggesting a physiological role of circulating AGF secreted from liver in antagonizing obesity.

Angptl3 is a circulating factor from liver functioning to regulate lipid metabolism[14,15]. Angptl4 is also predominantly expressed in liver and adipose tissue, and its expression is altered in nutrition and fasting, suggesting a role for Angptl4 in regulating fat metabolism[12,13]. Here, we show that AGF is a new hepatocyte-derived circulating factor counteracting high-fat-induced obesity and related insulin resistance through increased energy expenditure. Taken together with these findings, members of Angptl family function as endocrine factors with overlapping function secreted mainly from the liver to regulate metabolic homeostasis. As a next step to understand the role of Angptl family members in regulating metabolic homeostasis, identification of their cognate receptors and studies aimed at understanding their functional interactions are necessary.

In summary, we provide the first evidence that AGF directly antagonizes obesity and related insulin resistance. In addition to this direct effect, we propose that AGF-induced angiogenesis facilitates increased energy expenditure. Thus, AGF is a potential target for developing attractive pharmacological interventions counteracting obesity and related metabolic diseases.

METHODS

Gene targeting of *Angptl6*, generation of *Angptl6* transgenic mice, cell culture, transcription assays, western blot analyses and laser-Doppler blood flow analysis. Please see **Supplementary Methods** online.

Blood analysis and tissue triglyceride assay. For IGTT, female mice were deprived of food 16 h and given 0.75 mg glucose per g body weight intraperitoneally; 3-month-old *Angptl6*$^{-/-}$ mice and controls and 4-month-old *Angptl6* transgenic mice and controls were used ($n = 5$–6 each). For IITT, female mice were given 0.75 U human insulin per kg body weight by subcutaneous injection; 3-month-old *Angptl6*$^{-/-}$ mice and controls and 4-month-old *Angptl6* transgenic mice and controls were used ($n = 5$–6 each). Blood was withdrawn from the supraorbital vein at indicated times. Blood glucose was measured by glucose oxidase method (Sanwa Kagaku). Serum FFA, triglyceride and cholesterol levels were determined by nonesterified fatty acid C-test, triglyceride L-type and cholesterol L-type (Wako), respectively. Plasma insulin was measured by insulin immunoassay (Eiken Kagaku).

Leptin, adiponectin and TNF-α were assayed by leptin assay kit (Linco Research Inc.), ELISA-based adiponectin immunoassay kit (Otsuka Seyaku) and ELISA-based TNF-α immunoassay kit (Techne Corporation), respectively, according to the manufacturer's instructions. Tissues were excised, weighed and homogenized. We added 500 μl of homogenates to 3 ml of methanol/chloroform at 1:2 (vol/vol). The mixture was shaken for 10 min and then centrifuged. We removed the organic layer and saved it, and re-extracted the aqueous layer with 3 ml of methanol/chloroform, and evaporated a small aliquot of the combined organic extracts. The triglyceride concentration of this aliquot was determined as described earlier.

Physiological measurements. For measurement of food consumption, 6-month-old *Angptl6*$^{-/-}$ mice and controls (n = 8 each), and 5-month-old *Angptl6*-transgenic mice and controls (n = 10 each) were housed individually. We measured consumption of food, as well as body weight, for 7 d consecutively. Mice were fed a normal chow diet (CE-2) or a high-fat diet (HFD-32) (CLEA). The high-fat diet study with 6-week-old *Angptl6* transgenic mice and controls was followed for a period of 12 weeks. Rectal temperature was monitored (6-month-old *Angptl6*$^{-/-}$ mice and controls (n = 8 each), and 5-month-old *Angptl6*-transgenic mice and nontransgenic control mice (n = 10 each)) using an electronic thermistor (Model BAT-12) equipped with a rectal probe (RET-3, Physitemp). Oxygen consumption (VO_2) was determined in 6-month-old *Angptl6*$^{-/-}$ mice and controls (n = 5 each), and 5-month-old *Angptl6*-transgenic mice and controls (n = 12 each), with an O_2/CO_2 metabolic measuring system (Model MK-5000, Muromachikikai) at 24 °C as described elsewhere[41]. Mice were kept unrestrained in the chamber for 24 h without food. We determined VO_2 when the minimum plateau shape was obtained during the light cycle, which corresponded to the period of sleep or inactivity. VO_2 is expressed as the volume of O_2 consumed per kilogram weight of lean body mass per minute.

Quantitative RT-PCR. Total RNA was isolated from the BAT and musculus gastrocnemius of mice (6-month-old *Angptl6*$^{-/-}$ mice and controls (n = 5 each), and 6-month-old *Angptl6*-transgenic mice and controls (n = 5 each)). Preparation of DNase-treated total RNA, reverse transcription, and PCR protocols were performed as previously described[8]. The oligonucleotides used for PCR are listed in **Supplementary Table 1** online. We monitored the levels of PCR products with an ABI PRISM 7700 sequence detection system and analyzed them with ABI PRISM 7700 SDS software (Applied Biosystems JAPAN Ltd). The relative abundance of transcripts was normalized to constitutive expression of 18sRNA, β-actin or HPRT mRNA.

CT scan analysis. The adiposity of mice was examined radiographically using CT (LaTheta, ALOKA) according to the manufacturer's protocol. We performed CT scanning at 2-mm intervals from the diaphragm to the bottom of the abdominal cavity.

Hepatic overexpression of AGF by adenoviral transduction. To prepare high-fat diet–induced obese mice, 8-week-old C57BL/6 female mice were fed a high-fat diet containing 32% (wt/wt) fat (HFD-32) for 12 months. Subsequently, mice with high-fat diet–induced obesity (n = 8) received 5×10^9 plaque-forming units (p.f.u.) of Ad-AGF. Serum AGF level was elevated by a single injection of Ad-AGF. For controls, mice with high-fat diet–induced obesity (n = 8) received 5×10^9 p.f.u. of Ad-GFP at the same time. We monitored body weight and food intake daily after intravenous injection of Ad-AGF and Ad-GFP. On day 16 after injection, random fed blood glucose levels were examined. Subsequently, IITT was performed. On day 20 after injection, we examined levels of serum AGF and fasting blood glucose. Subsequently, IGTT was performed.

Statistical analysis and ethical considerations. Results are expressed as the mean ± s.d. or mean ± s.e.m. Differences between groups were examined for statistical significance using Student t test or analysis of variance (ANOVA) with Fisher's PLSD test. The Ethics Review Committee for Animal Experimentation of Keio University approved the experimental protocol.

Note: Supplementary information is available on the Nature Medicine website.

ACKNOWLEDGMENTS

We thank K. Fukushima for her assistance with the experiments. This work was supported by Grants-in-Aid for Scientific Research on Priority Areas from the Ministry of Education, Science and Culture of Japan, by the Yamanouchi Foundation for Research on Metabolic Disorders and by the Mochida Memorial Foundation for Medical and Pharmaceutical Research.

COMPETING INTERESTS STATEMENT

The authors declare competing financial interests (see the *Nature Medicine* website for details).

Received 4 July 2004; accepted 25 January 2005
Published online at http://www.nature.com/naturemedicine/

1. Spiegelman, B.M. & Flier, J.S. Obesity and the regulation of energy balance. *Cell* **104**, 531–543 (2001).
2. Matsuzawa, Y., Funahashi, T. & Nakamura, T. Molecular mechanism of metabolic syndrome X: Contribution of adipokines adipocyte-derived bioactive substances. *Ann. NY Acad. Sci.* **832**, 146–154 (1999).
3. Lowell, B.B., & Spiegelman, B.M. Towards a molecular understanding of adaptive thermogenesis. *Nature* **404**, 652–660 (2000).
4. Levine, J.A., Eberhardt, N.L., & Jensen, M.D. Role of nonexercise activity thermogenesis in resistance to fat gain in human. *Science* **283**, 212–214 (1999).
5. Gale, N.W., & Yancopoulos, G.D. Growth factors acting via endothelial cell-specific receptor tyrosine kinases: VEGFs, Angiopoietins, and ephrins in vascular development. *Genes Dev.* **13**, 1055–1066 (1999).
6. Oike, Y. *et al.* Angiopoietin-related/like protein (ARPs/Angptls) regulate angiogenesis. *Int. J. Hematol* **80**, 21–28 (2004).
7. Oike, Y. *et al.* Angiopoietin-related growth factor (AGF) promotes epidermal proliferation, remodeling and regeneration. *Proc. Natl. Acad. Sci. USA.* **100**, 9494–9499 (2003).
8. Oike, Y. *et al.* Angiopoietin-related growth factor (AGF) promotes angiogenesis. *Blood* **103**, 3760–3766 (2004).
9. Kim, I. *et al.* Molecular cloning, expression, and characterization of angiopoietin-related protein. *J. Biol. Chem.* **274**, 26523–26528 (1999).
10. Camenisch, G. *et al.* ANGPTL3 stimulates endothelial cell adhesion and migration via Integrin αvβ3 and induces blood vessel formation *in vivo*. *J. Biol. Chem.* **277**, 17281–17290 (2002).
11. Ito, Y. *et al.* Inhibition of angiogenesis and vascular leakiness by Angiopoietin-related protein 4. *Cancer Res.* **63**, 6651–6657 (2003).
12. Yoon, J.C. *et al.* Peroxisome proliferator-activated receptor gamma target gene encoding a novel angiopoietin-related protein associated with adipose differentiation. *Mol. Cell Biol.* **20**, 5343–5349 (2000).
13. Kersten, S, *et al.* Characterization of the fasting-induced adipose factor FIAF, a novel peroxisome proliferator-activated receptor target gene. *J. Biol. Chem.* **275**, 28488–28493 (2000).
14. Koishi, R, *et al.* Angptl3 regulates lipid metabolism in mice. *Nat. Genet.* **30**, 151–157 (2002).
15. Inaba, T, *et al.* Angiopoietin-like protein 3 mediates hypertriglyceridemia induced by the liver X receptor. *J. Biol. Chem.* **278**, 21344–21351 (2003).
16. Evans, R.M., Barish, G.D. & Wang, Y.X. PPARs and the complex journey to obesity. *Nat. Med.* **10**, 355–361 (2004).
17. Spiegelman, B.M. & Flier, J.S. Adipogenesis and obesity: Rounding out the big picture. *Cell* **87**, 377–389 (1996).
18. Uysal, K.T., Wiesbrock, S.M., Marino, M.W. & Hotamisligil, G.S. Protection from obesity-induced insulin resistance in mice lacking TNF-α function. *Nature* **389**, 610–614 (1997).
19. Peraldi, P., Xu, M. & Spiegelman, B.M. Thiazolidinediones block tumor necrosis factor-a-induced inhibitor of insulin signaling. *J. Clin. Invest.* **100**, 1863–1869 (1997).
20. Yamauchi, T. *et al.* The fat-derived hormone adiponectin reverses insulin resistance associated with both lipoatrophy and obesity. *Nat. Med.* **7**, 941–946 (2001).
21. Berg, A.H., Combs, T.P., Du, X., Brownlee, M. & Scherer, P.E. The adipocyte-secreted protein Acrp30 enhances hepatic insulin action. *Nat. Med.* **7**, 647–653 (2001).
22. Shimomura, I., Hammer, R.E., Ikemoto, S., Brown, M.S. & Goldstein, J.L. Leptin reverses insulin resistance and diabetes mellitus in mice with congenital lipodystrophy. *Nature* **401**, 73–76 (1999).
23. Friedman, J.M. Obesity in the new millennium. *Nature* **404**, 632–634 (2000).
24. Lowell, B.B., *et al.* Development of obesity in transgenic mice after genetic ablation of brown adipose tissue. *Nature* **366**, 740–742 (1993).
25. Zurlo, F., Larson, K., Bogardus, C. & Ravussin, E. Skeletal muscle metabolism is a major determinant of resting energy expenditure. *J. Clin. Invest.* **86**, 1423–1427 (1990).
26. Kamei, Y. *et al.* PPARγ coactivator 1β/ERR ligand 1 is an ERR protein ligand, whose expression induces a high-energy expenditure and antagonizes obesity. *Proc. Natl. Acad. Sci. USA.* **100**, 12378–12383 (2003).
27. Niwa, H., Yamamura, K. & Miyazaki J. Efficient selection for high-expression transfectants with a novel eukaryotic vector. *Gene* **108**, 193–200 (1991).
28. Sierra-Honigmann, M.R. et al. Biological action of leptin as an angiogenic factor. *Science* **281**, 1683–1686 (1998).
29. Sarmiento, U., *et al.* Morphologic and molecular changes induced by recombinant human leptin in the white and brown adipose tissues of C57BL/6 mice. *Lab. Invest.* **77**, 243–256 (1997).
30. Shimomura, I. *et al.* Insulin resistance and diabetes mellitus in transgenic mice expressing nuclear SREBP-1c in adipose tissue: model for congenital generalized lipodystrophy. *Genes Dev.* **12**, 3182–3194 (1998).
31. Gavrilova, O. *et al.* Surgical implantation of adipose tissue reverses diabetes in

lipoatrophic mice. *J. Clin. Invest.* **105**, 271–278 (2000).
32. Moller, D.E. & Berger, J.P. Role of PPARs in the regulation of obesity-related insulin sensitivity and inflammation. *Int. J. Obes. Relat. Metab. Disord.* **27**, S17–S21 (2003).
33. Wu, Z., *et al.* Mechanisms controlling mitochondrial biogenesis and respiration through the thermogenic coactivator PGC-1. *Cell* **98**, 115–124 (1999).
34. Puigverger, P. *et al.* Cytokine stimulation of energy expenditure through p38 MAP kinase activation of PPARγ coactivator-1. *Mol. Cell* **8**, 971–982 (2001).
35. Puigserver, P. & Spiegelman, B.M. Peroxisome proliferator-activated receptor-γ coactivator 1α (PGC-1α): Transcriptional coactivator and metabolic regulator. *Endocr. Rev.* **24**, 78–90 (2003).
36. Wang, Y.X. *et al.* Peroxisome-proliferator-activated receptor δ activates fat metabolism to prevent obesity. *Cell* **113**, 159–70 (2003).
37. Tanaka, T. *et al.* Activation of peroxisome proliferator-activated receptor delta induces fatty acid beta-oxidation in skeletal muscle and attenuates metabolic syndrome. *Proc. Natl. Acad. Sci. USA.* **100**, 15924–15929 (2003).
38. Dressel, U. *et al.* The peroxisome proliferatior-activated receptor β/δ agonist, GW501516, regulates the expression of genes involved in lipid catabolism and energy uncoupling in skeletal muscle cells. *Mol. Endocrinol.* **17**, 2477–2493 (2003).
39. Shulman, G.I., *et al.* Cellular mechanisms of insulin resistance. *J. Clin. Invest.* **106**, 171–176 (2000).
40. Petersen, K.F. *et al.* Mitochondrial dysfunction in the elderly: Possible role in insulin resistance. *Science* **300**, 1140–1142 (2003).
41. Barger, P.M., Browning, A.C., Garner, A.N. & Kelly, D.P. p38 mitogen-activated protein kinase activates peroxisome proliferator-activated receptor α: a potential role in the cardiac metabolic stress response. *J. Biol. Chem.* **276**, 44495–44501 (2001).

MOLECULAR AND CELLULAR BIOLOGY, Aug. 2005, p. 6694–6706 Vol. 25, No. 15
0270-7306/05/$08.00+0 doi:10.1128/MCB.25.15.6694–6706.2005

Mammalian Polyhomeotic Homologues Phc2 and Phc1 Act in Synergy To Mediate Polycomb Repression of *Hox* Genes

Kyo-ichi Isono,[1,2] Yu-ichi Fujimura,[1,2] Jun Shinga,[1,2] Makoto Yamaki,[2] Jiyang O-Wang,[1] Yoshihiro Takihara,[3] Yasuaki Murahashi,[1,2] Yuki Takada,[1,2] Yoko Mizutani-Koseki,[1,2] and Haruhiko Koseki[1,2]*

RIKEN Research Center for Allergy and Immunology, 1-7-22 Suehiro, Tsurumi-ku, Yokohama 230-0045, Japan[1]; Department of Molecular Embryology, Graduate School of Medicine, Chiba University, 1-8-1 Inohana, Chuo-ku, China 260-8670, Japan[2]; and Department of Stem Cell Biology, Research Institute for Radiation Biology and Medicine, Hiroshima University, 1-2-3 Kasumi, Minami-ku, Hiroshima 734-8553, Japan[3]

Received 2 December 2004/Returned for modification 27 January 2005/Accepted 4 May 2005

The Polycomb group (PcG) gene products form multimeric protein complexes and contribute to anterior-posterior (A-P) specification via the transcriptional regulation of *Hox* cluster genes. The *Drosophila polyhomeotic* genes and their mammalian orthologues, *Phc1*, *Phc2*, and *Phc3*, encode nuclear proteins that are constituents of evolutionarily conserved protein complexes designated class II PcG complexes. In this study, we describe the generation and phenotypes of *Phc2*-deficient mice. We show posterior transformations of the axial skeleton and premature senescence of mouse embryonic fibroblasts associated with derepression of *Hox* cluster genes and *Cdkn2a* genes, respectively. Synergistic actions of a *Phc2* mutation with *Phc1* and *Rnf110* mutations during A-P specification, coimmunoprecipitation of their products from embryonic extracts, and chromatin immunoprecipitation by anti-Phc2 monoclonal antibodies suggest that *Hox* repression by Phc2 is mediated through the class II PcG complexes, probably via direct binding to the *Hox* locus. The genetic interactions further reveal the functional overlap between *Phc2* and *Phc1* and a strict dose-dependent requirement during A-P specification and embryonic survival. Functional redundancy between Phc2 and Phc1 leads us to hypothesize that the overall level of polyhomeotic orthologues in nuclei is a parameter that is critical in enabling the class II PcG complexes to exert their molecular functions.

The Polycomb group (PcG) genes were originally identified through their requirement in the maintenance of the stable repression of *Hox* genes during the development of *Drosophila melanogaster* (34, 38). The products of these *Drosophila* PcG genes form large multimeric protein complexes in the chromatin. It is thought that they stably repress the target genes by altering the configuration of the chromatin, as suggested by the synergistic genetic interactions between mutant alleles of different *Drosophila* PcG genes (15, 39).

PcG genes that are structurally and functionally related to those found in *Drosophila* have also been identified in mammals, where their products form at least two distinct functional complexes. One complex, designated the class I PcG complex, comprises the products of the embryonic endoderm development (Eed) (the orthologue of the *Drosophila extra sex combs* gene) and the Enx1 and Enx2 (the orthologues of the *Drosophila enhancer of zeste* gene) PcG genes. Since the SET domains of Enx1 and Enx2 function as histone methyltransferases, and Eed interacts with histone deacetylases, this complex is believed to alter chromatin structures by modifying core histone tails (35, 46). The second complex, designated class II, is closely related to the Polycomb repressive complex 1 (PRC1) in *Drosophila* and includes the products of the paralogues of another subset of PcG genes in HeLa cell extracts, designated hPRC-H (27, 39). This subset contains the following gene groups: *Rnf110* (*Mel18*) and *Bmi1*; *Cbx2* (*M33*), *Cbx4* (*Pc2*), and *Cbx8* (*Pc3*); *Phc1* (*rae28*, *mph1*, or *edr1*), *Phc2* (*mph2* or *edr2*), and *Phc3*; and *Ring1A* and *Rnf2* (*Ring1B*) (27). Apart from *Rnf2* mutants, mice that are deficient in the individual components of class II PcG complexes display anterior shifts in the expression boundaries of *Hox* cluster genes in the paraxial mesoderm and neural tube and, in general, characteristically show posterior transformation of the axial skeleton. These mutant mice also invariably display severe combined immunodeficiency due to increased apoptosis and a lack of proliferative responses of hemopoietic cells via regulation of the Cdkn2a/p53 pathway (1, 2, 11, 13, 19, 21, 40, 41, 45, 47). There is accumulating biochemical and genetic evidence to indicate that the class II PcG complexes are compositionally and functionally conserved between flies and mammals. Nevertheless, many PcG genes have also diverged substantially, and most are either duplicated or triplicated in mammals (27, 39).

In *Drosophila*, the *polyhomeotic* (*ph*) locus consists of *polyhomeotic-proximal* (*ph-p*) and *polyhomeotic-distal* (*ph-d*) sequences, which have extensive homology. Three mammalian genes homologous to *ph*, *Phc1*, *Phc2*, and *Phc3*, have been identified (14, 16, 27, 32, 44). Database screening revealed that all three *ph* orthologues were evolutionarily conserved and expressed in various vertebrates, including humans, chickens, zebra fish, and fugu (Y. Murahashi and H. Koseki, unpublished data). Comparisons of the ph proteins and their vertebrate orthologues have shown that each has a single FCS finger [also

* Corresponding author. Mailing address: RIKEN Research Center for Allergy and Immunology, 1-7-22 Suehiro, Tsurumi-ku, Yokohama 230-0045, Japan. Phone: 81-45-503-9689. Fax: 81-45-503-9688. E-mail: koseki@rcai.riken.jp.

called the (Cys)4-type Zn coordination domain] flanked by two additional conserved domains. The function of the upstream motif, described as homology domain I (HDI), is unknown. However, the downstream homology domain II (HDII), which is located at the C-terminal end, has been described as a sterile alpha motif (SAM) domain (also known as SEP or SPM) (4, 16). Recently, the FCS finger domain of Phc1 has been shown to encode an RNA binding motif and to regulate subnuclear localization when tested in *Caenorhabditis elegans* (50). The SAM domains are found at the C-terminal ends, not only of ph proteins and their mammalian orthologues, but also on the *Drosophila* Sex comb on the midleg (SCM) gene and its orthologues as a component of PcG proteins (8, 42). It has been shown that the SAM domains are able to self-associate, bind to other SAM domains, and form heterotypic interactions with non-SAM domain domain-containing proteins (23, 32, 38). Importantly, ph-SAM has been shown to form a helical polymer structure, which provides a possible mechanism for the extension of PcG complexes (23). This finding is in close agreement with the recent biochemical observation that Phc1 plays a pivotal role in mediating the PcG-dependent bridging of distant chromatin templates (26). Coimmunoprecipitation of mammalian ph orthologues from HeLa and U-2 OS cell extracts suggests that the heterophilic polymerization of the SAM domains of Phc1, Phc2, and Phc3 may be involved in mediating PcG-dependent regulatory mechanisms via higher-order chromatin structures (16, 27).

However, the molecular complicity among mammalian ph orthologues has not yet been addressed due, at least in part, to a lack of *Phc2* or *Phc3* mutant alleles. In this study, we describe the generation and phenotypes of *Phc2*-deficient mice. Using these mutants, we studied the biochemical and genetic evidence that supports the involvement of Phc2 as a functional component of class II PcG complexes during embryogenesis.

MATERIALS AND METHODS

Production of anti-Phc2 monoclonal antibody. A partial cDNA fragment that encodes from N22 to the stop codon of Phc2 was subcloned into the pGEX vector to express a glutathione *S*-transferase–Phc2 fusion protein. This fusion protein was purified and injected several times into female BALB/c mice to generate a hybridoma, which was screened as described previously (5).

IP and immunoblotting. Monoclonal antibodies to Phc2, Phc1, and Rnf2 (in 30 μl, 100 μl, and 30 μl of culture supernatant, respectively) and 5 μg of a polyclonal antibody to Rnf110 (C-20; Santa Cruz Biotechnology, Santa Cruz, CA) were conjugated with 50% (vol/vol) protein G-Sepharose (25 μl) in 300 μl of buffer (20 mM HEPES [pH 7.8], 20 mM NaCl, 0.2 mM EDTA, 1 mM dithiothreitol, and 0.01% Triton X-100) at 4°C for at least 2 h (5, 28). A mouse embryo at 11.5 days postcoitus (dpc) was sonicated three times for 10 s in immunoprecipitation (IP) buffer (400 μl), consisting of 20 mM HEPES (pH 7.8), 10% (vol/vol) glycerol, 150 mM NaCl, 0.2 mM EDTA, 1 mM dithiothreitol, and 2 mM Pefabloc SC (Roche Molecular, Indianapolis, IN). After centrifugation, the supernatant was precleared with 50 μl of 50% (vol/vol) protein G-Sepharose for 60 min and then incubated with each of the three Sepharose-conjugated antibodies for 90 min at 4°C. The Sepharose-bound proteins were washed five times with 800 μl of IP buffer without Pefabloc SC, boiled in sodium dodecyl sulfate sample buffer, separated on 9% denaturing polyacrylamide gels, and subjected to immunoblot analysis.

Generation of *Phc2*-deficient mice. To generate *Phc2*-deficient mice, a targeting vector was constructed (see Fig. 2A). This vector was introduced into R1 embryonic stem cells as described previously, and five homologous recombinants were obtained (31). *Phc2*$^{+/-}$ mice were backcrossed six times onto a C57BL/6 background, and homozygotes were generated by mating between heterozygotes. *Phc2*$^{+/-}$ mice were crossed with *Phc1*$^{+/-}$ and *Rnf110*$^{+/-}$ mice, after backcrossing to C57BL/6 a few times, to generate double heterozygotes. These *Phc2*$^{+/-}$-*Phc1*$^{+/-}$ and *Phc2*$^{+/-}$-*Rnf110*$^{+/-}$ mice were viable and fertile. In order to generate *Phc2-Phc1* double homozygotes, double heterozygotes were crossed. For the generation of *Phc2-Rnf110* double homozygotes, we first generated *Phc2*$^{-/-}$-*Rnf110*$^{+/-}$ mice, which were again viable and fertile, and crossed them to either *Phc2*$^{+/-}$-*Rnf110*$^{+/-}$ or *Phc2*$^{-/-}$-*Rnf110*$^{+/-}$ mice. All animal experiments were carried out according to the in-house guidelines for the care and use of laboratory animals of the Riken Research Center for Allergy and Immunology, Yokohama, Japan.

Morphological analyses. Skeletal preparations were prepared from either perinatal or late-gestational mice as described previously (22). In situ hybridization on tissue sections and whole-mount in situ hybridization were performed as described previously (22, 48).

Cell culture conditions. Mouse embryonic fibroblasts (MEFs) were prepared from each genotype using 13.5- to 14.5-dpc fetuses and maintained according to a 3T9 protocol (20). The proliferation of MEFs was investigated at passage 5 by plating 10^4 cells per 60-mm-diameter dish in replicate cultures and then counting the cells from duplicate cultures every other day. This experiment was repeated four times, using MEFs derived from eight homozygous mutants and six wild types; almost identical results were obtained for each of the four repeats.

Chromatin immunoprecipitation (ChIP). Using scissors, the embryonic tissues were minced on ice and then subjected to chemical cross-linking by incubating them in 1% formaldehyde in phosphate-buffered saline for 10 min at room temperature. After extensive sonication, the chromatin fractions were purified by CsCl isopycnic centrifugation (33); 10 mM NaCl and 0.1% NP-40 were added to the purified fractions in order to perform optimal immunoprecipitation of the anti-Phc2 antibody. Precleared protein extracts were then incubated with rocking, with 40 μl of anti-Phc2 culture supernatant per 200 μl lysate, at 4°C from 2 h to overnight. Immune complexes were captured by incubating them for 3 h with protein A-Sepharose beads.

To isolate genomic DNA from these immune complexes, the beads were treated with 50 μg/ml of RNase A at 37°C for 30 min, followed by incubation overnight with 500 μg/ml proteinase K-0.5% sodium dodecyl sulfate at 37°C. After being heated for several hours at 65°C to achieve reverse cross-linking, the supernatants were collected, extracted by phenol-chloroform, and concentrated by ethanol precipitation. Genomic DNA was also isolated from the original unfractionated chromatin by the same procedure described above and designated "input" DNA. To measure the DNA yield, aliquots of immunoprecipitated DNA were electrophoresed on an agarose gel next to serially diluted input DNA.

We carried out semiquantitative PCR using serially diluted input DNA and immunoprecipitated DNA as templates. The enrichment of DNA by immunoprecipitation was estimated from the band intensities of the gel images. This series of experiments were all performed at least three times and gave similar results. The following primer pairs were used in this study: *p16* first exonic region, 5′-CGAACTCGAGGAGAGCCATC-3′ and 5′-ACACTCCTTGCCTACCTGAA-3′; common second exonic regions of *p16/p19*ARF, 5′-TCACGTAGCAGCTCTTCTGC-3′ and 5′-CAGCGGAACGCAAATATCGC-3′; *Hoxb8* enhancer region (BH1100), 5′-GGGTATAAATTTCTGAAGGTTAAG-3′ and 5′-AGGGATGAGAAGGGCCGAGGG-3′; *Hoxb8* promoter region, 5′-TATGACTACCTCGTTGTTTG-3′ and 5′-CAAAGACTGATGTGGGGGAGT-3′; *Hoxb8* intronic region, 5′-CCCTGGATGCGCCCTCAAG-3′ and 5′-TCTCCACAGCCCCCATAAAAC-3′; *Hoxb7* enhancer region (KA), 5′-CTCCTTCCCTTCTCTTGGGGGTCC-3′ and 5′-CAATGCTCACAGCGCGCATGC-3′; and *Adam34* coding region, 5′-ATGAGTGGGACTAAGGCCCTG-3′ and 5′-GCGGTTATGATCTATTACTAC-3′.

Isolation of lymphocyte subpopulations at distinct stages of development. Bone marrow cells derived from C57BL/6 mice were stained with allophycocyanin-labeled B220, phycoerythrin (PE)-labeled anti-CD43, and fluorescein isothiocyanate (FITC)-labeled anti-immunoglobulin M (IgM). Populations of B220$^+$ CD43$^+$ IgM$^-$ (pro-B), B220$^+$ CD43$^-$ IgM$^-$ (pre-B), and B220^{dull} CD43$^-$ IgM$^+$ (immature B) cells were isolated with a Vantage fluorescence-activated cell sorter (BD Biosciences, Mountain View, CA). Similarly, thymocytes were stained with FITC-labeled CD4 and PE-labeled CD8 antibodies, and the CD4$^-$ CD8$^-$, CD4$^+$ CD8$^+$, CD4$^+$ CD8$^-$, and CD4$^-$ CD8$^+$ subpopulations were sorted. To isolate immature and mature B cells, splenocytes were stained with FITC-labeled B220 and PE-labeled AA4 antibodies, and B220$^+$ AA4$^+$ (immature B) and B220$^+$ AA4$^-$ (mature B) cells were sorted. To purify the different mature-B-cell populations, splenocytes were stained with allophycocyanin-labeled B220, FITC-labeled CD21, and PE-labeled CD23 antibodies, and B220$^+$ CD21$^-$ CD23$^+$ (follicular B), B220$^+$ CD21$^+$ CD23^{dull} (marginal-zone B), and B220$^+$ CD21$^-$ CD23$^-$ (newly formed B) cells were sorted. To isolate germ center B cells, mice were immunized with 100 μg of 2,4-dinitrofluorobenzene-conjugated ovalbumin in alum. Twelve days after immunization, spleen cells were stained with PE-labeled B220, and FITC-labeled peanut agglutinin

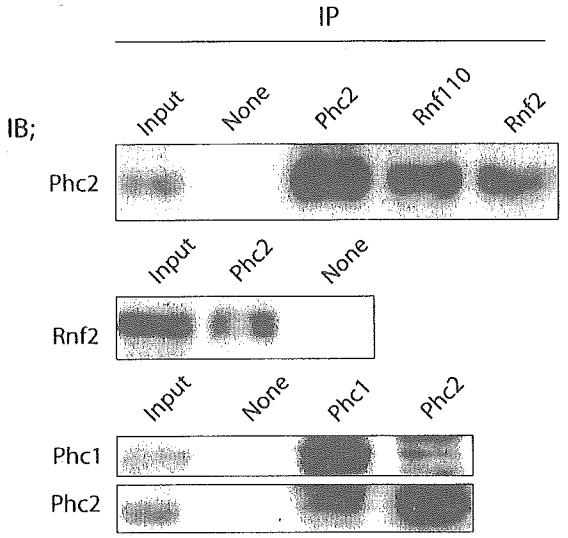

FIG. 1. Association of Phc2 with other components of class II PcG complexes during embryogenesis. Antibodies used for IP and immunoblotting (IB) are indicated over each lane and beside each blot, respectively. Phc2 was coimmunoprecipited with Rnf110, Rnf2, and Phc1 from 11.5-dpc embryonic extracts. Original whole-cell extract was loaded on the lanes labeled "Input"; mock immunoprecipitation without primary antibody was performed as a negative control on the lanes labeled "None."

(PNA) and B220$^+$ PNA$^+$ cells were sorted using a high-speed cell sorter (Aria; BD Biosciences). The sorted cells were dissolved in Trizol reagent (Invitrogen, Carlsbad, CA), and total RNA was extracted according to Invitrogen's protocol.

RT-PCR analysis. Mouse total-RNA panels were purchased from BD Biosciences. First-strand cDNA was synthesized from 2 μg of the total RNA using SuperScript III réverse transcriptase (RT) (Invitrogen) and random primers, according to the manufacturer's protocol. The forward and reverse primers for PCR were 5′-CCTACAAGTTCAAGCGTTCC-3′ and 5′-GTCCCTCATGTGC ATGTCAG-3′ for mouse *Phc2*, 5′-GACAGGCTAGCTCCCCAAAC-3′ and 5′-GCTAGGGCCTGGCTAGAAGT-3′ for *Phc1*, and 5′-ATGGATGACGATAT CGCT-3′ and 5′-ATGAGGTAGTCTGTCAGGT-3′ for β-*actin* genes. The amplification conditions were 95°C for 10 s, 60°C for 20 s, and 72°C for 1 min for 30 cycles for both *Phc2* and *Phc1* genes and 95°C for 5 s, 54°C for 10 s, and 72°C for 1 min for 25 cycles for β-*actin* genes.

RESULTS

Association of Phc2 with the hPRC-H-like complex during embryogenesis. To address whether Phc2 is involved in a multimeric protein complex similar to hPRC-H during mouse embryogenesis (27), we raised a monoclonal antibody against a glutathione *S*-transferase–Phc2 (N22 to the stop codon) fusion protein (K. Isono and H. Koseki, unpublished data). We used whole-cell extracts from 11.5-dpc embryos for the coimmunoprecipitation experiments, as mammalian PcG complexes are considered to be functional at this gestational stage, at least as demonstrated by the derepression of *Hox* gene expression (1, 41, 45). The anti-Phc2 monoclonal antibody recognized an ~40-kDa protein on the immunoblots of these 11.5-dpc embryonic extracts. The anti-Phc2 and goat anti-Rnf110 and anti-Rnf2 monoclonal antibodies were able to immunoprecipitate the Phc2 proteins from 11.5-dpc embryonic extracts (Fig. 1). Phc2 was not detected in the absence of these primary antibodies. Inclusion of Rnf2 in the Phc2 immunoprecipitates confirmed the result described above. The anti-Phc2 and -Phc1 monoclonal antibodies were both able to immunoprecipitate Phc1 and Phc2 in a reciprocal fashion. These results revealed the association of Phc2 with Rnf110, Rnf2, and Phc1 in 11.5-dpc embryos; this interaction has been shown previously in human osteosarcoma U-2 OS cells (16, 29, 49).

Generation of a Phc2 mutant allele. To examine the physiological roles of Phc2, we inactivated the *Phc2* locus by replacing the second and third exons with a neomycin resistance (*Neo*^{r}) gene cassette (Fig. 2A). This replacement was expected to delete the polypeptide stretch from the start codon to E95, which encodes the HDI region from the 36-kDa isoform. *Phc2* heterozygotes were backcrossed six times to C57BL/6 mice to eliminate the effects of genetic background, and then homozygotes were generated. Over 20 litters were genotyped either at birth or at weaning. Three genotypes were identified, which segregated into ratios according to the laws of Mendelian inheritance (Fig. 2B) (J. Shinga and H. Koseki, unpublished data). *Phc2*$^{-/-}$ mice were viable and fertile. Next, we examined the expression of *Phc2* in the homozygotes (Fig. 2C). Northern blot analysis, using total cellular RNA from 11.5-dpc embryos, revealed three aberrant transcripts in the homozygotes, with only a 2.5-kb band present in the wild type. At least two differently spliced transcripts appeared to be generated from the *Phc2* locus in the wild type, represented by a 2.5-kb and a very faint 3.8-kb transcript. Exons 2 to 7 were common to both, while exons 1 and 0 were unique to the 2.5- and 3.8-kb transcripts, respectively (49) (Fig. 2D, top). RT-PCR analysis identified the prospective 2.5- and 3.8-kb transcripts, which were missing the second and third exonic regions, as being expressed in the homozygous mutants (Fig. 2D, bottom). Since in these homozygotes, the putative start codon had been removed from the 2.5-kb transcript while the deletion of the second exonic region from the 3.8-kb transcripts resulted in the frameshift leading to premature termination, it is likely that Phc2 proteins were not produced or that a truncated protein starting from M128 of the 36-kDa isoform and lacking the HD1 and FCS finger might be expressed. Indeed, no signals were detected at around 40 kDa, or in the range of smaller molecular mass below, by immunoblot analysis, which used materials immunoprecipitated by the anti-Phc2 monoclonal antibody from 11.5-dpc embryos (Fig. 2E). Therefore, this *Phc2* mutant allele may be null or encode a truncated C-terminal polypeptide that could not be detected by the anti-Phc2 monoclonal antibody.

Homeotic transformations of the axial skeleton concomitant with derepression of Hox genes in Phc2 mutants. Common features shared by mammalian class II *PcG* mutants are homeotic transformations of the axial structures associated with derepression of *Hox* cluster genes and premature senescence of embryonic fibroblasts associated with the overexpression of *Cdkn2a* transcripts (19). Eighteen pups, obtained by mating homozygous males and heterozygous females, were analyzed. All homozygotes exhibited at least a few alterations to the axial skeleton that were characteristic of posterior transformations (Fig. 3A and C), whereas heterozygotes showed much lower penetrance (Shinga and Koseki, unpublished). These alterations were as follows: an ectopic bone floating between the occipital bones and the first cervical vertebra (C1); in the cervical region, an odontoid process (a characteristic feature of C2) was fused to C1, suggesting intermediate morphological features between C1 and C2 (Fig. 3A); and the dorsal part of

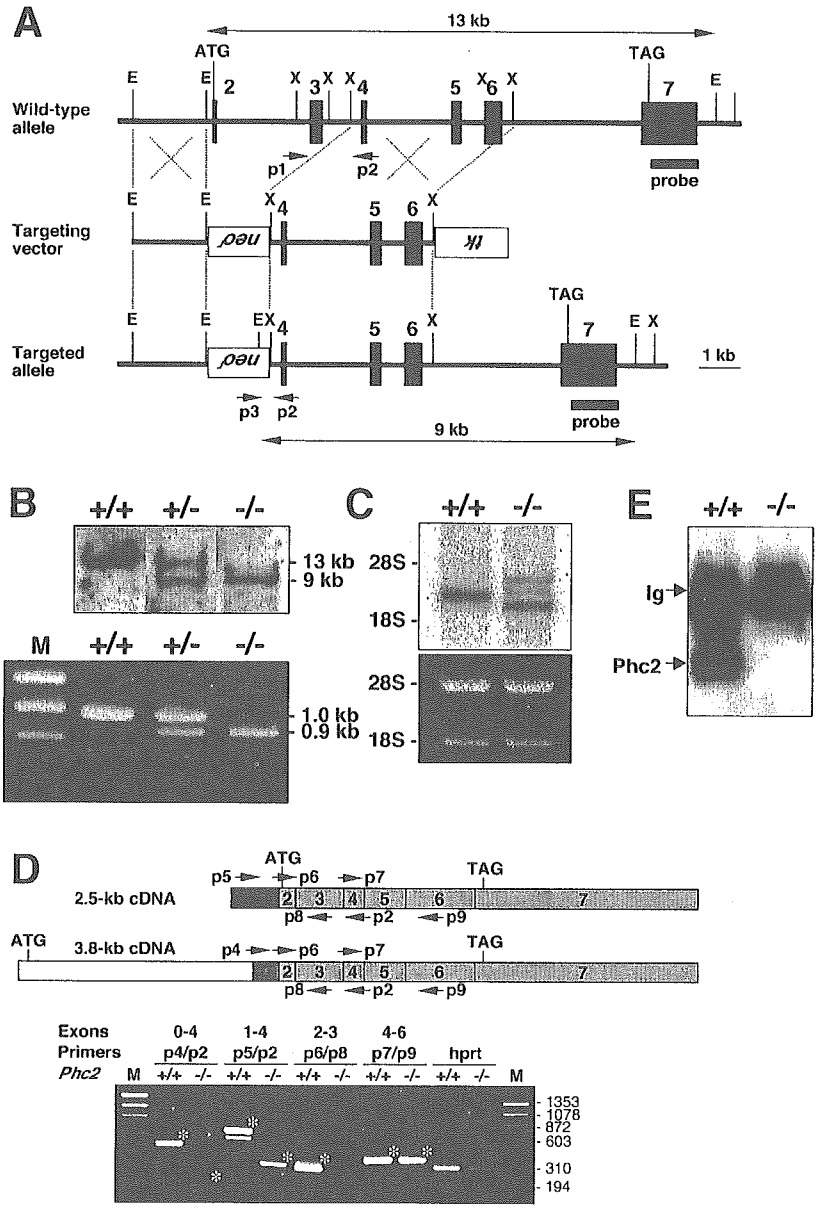

FIG. 2. Disruption of the *Phc2* gene in mice. (A) Diagram of the *Phc2* locus, the targeting vector, and the targeted allele. The PGKneo and pMC1-tk expression cassettes were used for positive and negative selection, respectively. The relevant positions of the restriction sites (EcoRI, E; XhoI, X), locations of the external probe and PCR primers, and sizes of diagnostic fragments are indicated. (B) Southern (top) and PCR (bottom) analyses for genotyping. For Southern blotting, genomic DNA was digested by EcoRI and probed with the 3′ probe, as indicated in panel A. For PCR, a mixture of three primers (p1, p2, and p3 in panel A) was used. Lane M, molecular size markers. (C) Northern analysis of *Phc2* expression in 11.5-dpc wild-type and homozygous embryos (top). Ethidium bromide staining of the same gel is shown below. (D) RT-PCR analysis of *Phc2* expression. The locations of the PCR primers are indicated on both the 2.5- and 3.8-kb transcripts (top). The asterisks indicate specific PCR products. Note the presence of truncated *Phc2* transcripts lacking exons 2 and 3. (E) Immunoprecipitation and immunoblot analyses of Phc2 expression in 11.5-dpc embryos.

C1 or C2 was often bifurcated in *Phc2* homozygotes (Fig. 3A). The lateral view of mutant C2 was similar to that of wild-type C3. In all homozygotes, ectopic ribs were associated with C7 (Fig. 3A). In 67% of cases, the ectopic ribs were imperfect and fused to the middle part of the first ribs, while in the remainder, perfect ribs were formed that were directly associated with the cranially shifted sternum. The prominent spinous process characteristic of the second thoracic vertebra (T2) in the wild type was associated with T1 in all homozygotes. In the rib cage, the 7th ribs were detached from the sternum and the 13th ribs were missing or floating (Fig. 3A). Similarly, the thoracolumbar and lumbosacral boundaries were shifted anteriorly in the homozygotes. No significant changes were seen in the skull.

Next, we examined the phenotypic expression of *Hoxb3*, *-b4*, *-b6*, *-c6*, *-d4*, and *-a5* (Fig. 4). The anterior boundary of *Hoxb3* expression at the first prevertebra in the wild type was shifted

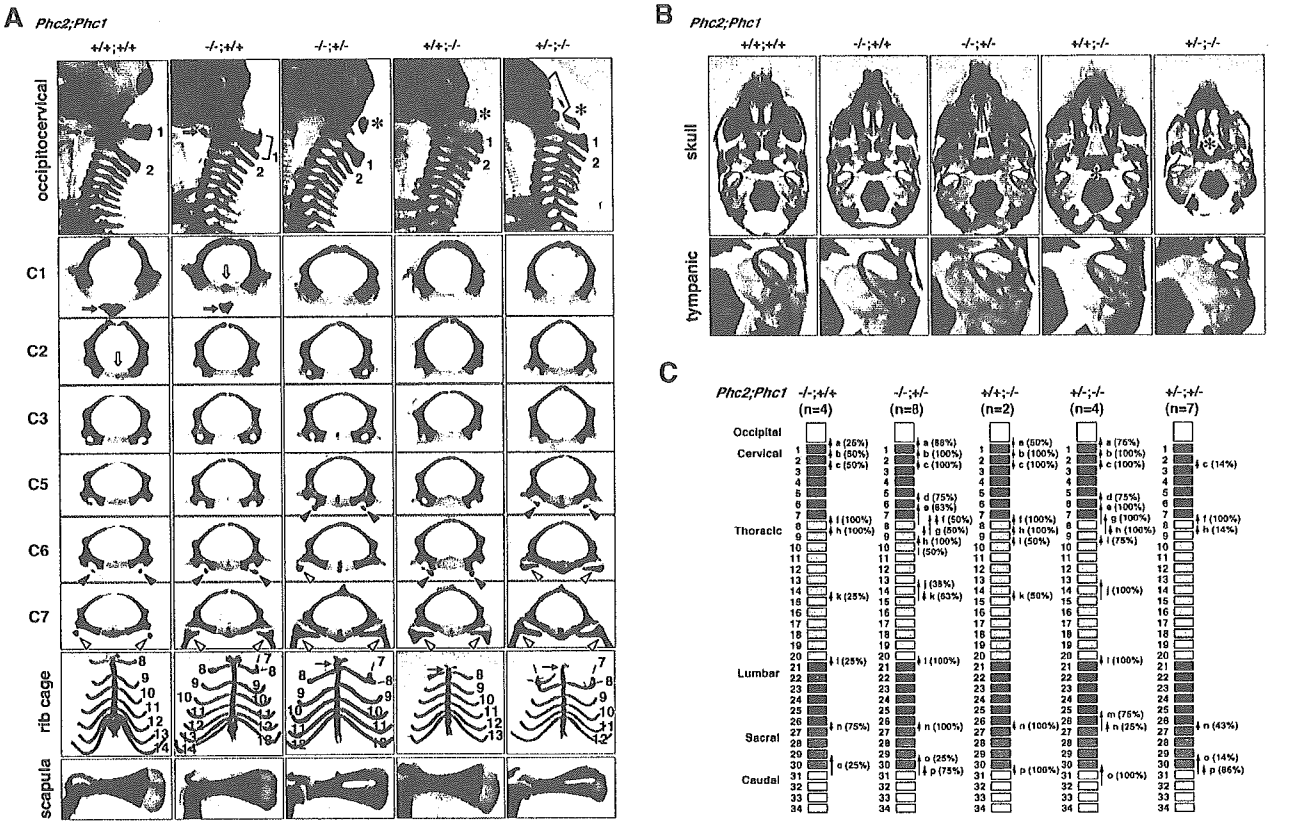

FIG. 3. Skeletal alterations in *Phc2*$^{-/-}$ mice and gene dose-dependent skeletal alterations in *Phc2-Phc1* compound mutants. (A) Lateral views of the occipitocervical region; overviews of individual C1, C2, C3, C5, C6, and C7 vertebrae; ventral views of rib cages; and overviews of scapulas. In the lateral views of the occipitocervical region, C1 and C2 are indicated numerically, and asterisks indicate the ectopic arch or piece. In *Phc2*$^{+/-}$*-Phc1*$^{-/-}$ mice, a bracket indicates the segmentation of the exoccipital bone and an arrow indicates the anterior tuberculus of C1. In C1 and C2 vertebrae, closed and open arrows, respectively, indicate the anterior tuberculus and odontoid processes. In C5, C6, and C7, closed and open arrowheads, respectively, indicate the anterior tuberculus for vertebral arteries and ectopic ribs. In ventral views of the rib cages, the numbers of vertebrae to which ribs are attached are indicated. (B) Ventral views of skulls and tympanic bones. In the skull, a cleft in the secondary palate is emphasized by the use of yellow lines indicating the medial edges of the palatine. Note the absence of cartilaginous condensation at the center of the sphenoid in *Phc2*$^{+/-}$*-Phc1*$^{-/-}$ mice. (C) Summary of posterior transformations. Each arrow represents the homeotic transformation of vertebrae. (a) Supraoccipital bone→C1, appearance of the ectopic arch or bone; (b) C1→C2, fusion of the odontoid process to the C1 vertebra; (c) C2→C3; (d) C5→C6, association of the anterior tuberculus with the C5 vertebra; (e) C6→T1, association of the cervical rib with the C6; (f) C7→T1, association of the cervical rib with C7; (g) C7→T2, prominent spinous process on C7; (h) T1→T2, prominent spinous process on T1; (i) T2→T3, lack of prominent spinous process in T2; (j) T6→T8, dissociation of the sixth rib from the sternum; (k) T7→T8, dissociation of the seventh rib from the sternum; (l) T13→L1, loss of the rib from the 20th vertebra; (m) L4→S1, formation of a sacroiliac joint in the 25th vertebra; (n) L6→S1, formation of a sacroiliac joint in the 26th vertebra; (o) S3→Ca1, appearance of the first caudal vertebra in the 29th vertebra; (p) S4→Ca1, appearance of the first caudal vertebra in the 30th vertebra.

cranially to reach the caudal part of the basioccipital bone anlage in *Phc2*$^{-/-}$ embryos. Similarly, the anterior boundaries of *Hoxb4*, *-b6*, *-c6*, and *-d4* were shifted cranially in *Phc2*$^{-/-}$ embryos, while *Hoxa5* was not. Therefore, this showed that Phc2 was involved in the anterior-posterior (A-P) specification of the vertebral column through the regulation of *Hox* gene expression, as well as other PcG proteins.

Premature senescence of MEFs in *Phc2* mutants. *Phc2*$^{-/-}$ MEFs exhibit defects in proliferation and premature senescence, as well as MEFs derived from *M33*, *Bmi1*, and *Rnf110* mutants (11, 19) (H. Koseki, unpublished data). Growth curves of MEFs from wild-type and *Phc2*$^{-/-}$ genotypes were compared, using a strict 3T9 protocol (20) (Fig. 5A). *Phc2*$^{-/-}$ MEFs grew more slowly than wild-type MEFs, even in early passages; they also stopped dividing earlier (passage 7 versus passage 15, respectively). The proliferation of *Phc2*$^{-/-}$ MEFs was clearly affected at passage 5 (Fig. 5B). These observations indicated that *Phc2*$^{-/-}$ MEFs senesced more quickly than the wild-type MEFs. This prompted us to examine the expression of the two *Cdkn2a* genes, *p16* and *p19*^{ARF}, and we found that their expression was clearly derepressed in *Phc2*$^{-/-}$ MEFs, even as early as passage 3 (Fig. 5C). Therefore, premature senescence induced by the *Phc2* mutation was shown to involve the activation of Cdkn2a gene products, as has been found for other *PcG* mutants (19). It is also known that some immunological defects seen in *Bmi1* mutants are mediated by the overexpression of Cdkn2a products (19). We did not see significant changes in lymphocyte development in *Phc2*$^{-/-}$ mice.

We then addressed whether the *Phc2* mutation had an impact on *Cdkn2a* expression by using ChIP to look at the phys-

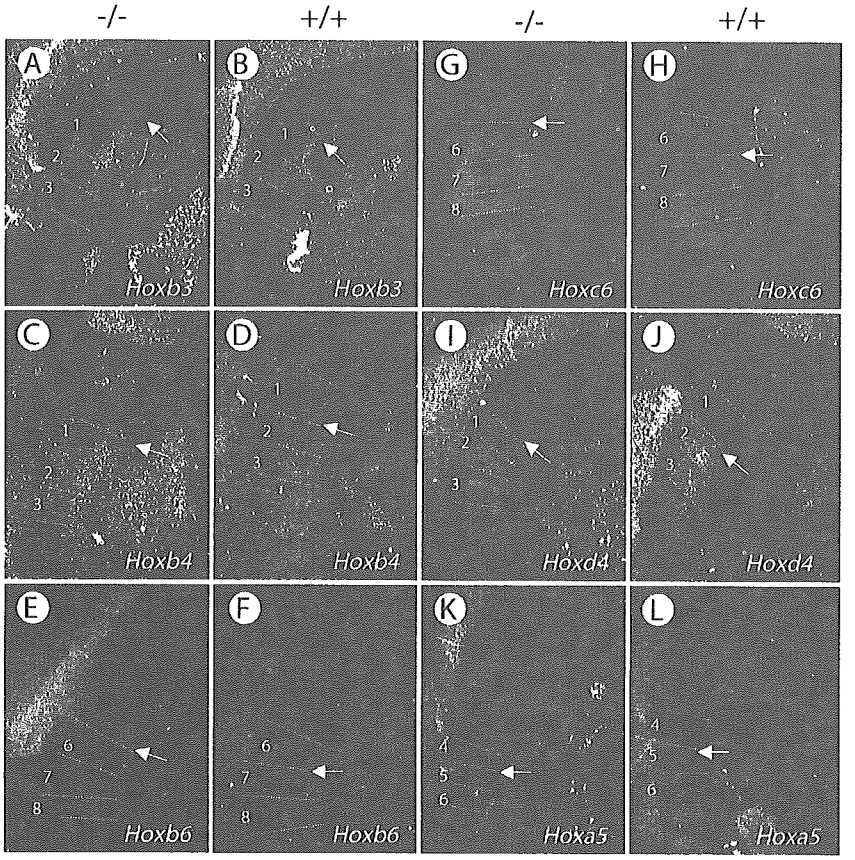

FIG. 4. Changes in *Hox* gene expression in *Phc2*$^{-/-}$ mice. Expression of *Hox* genes in 11.5-dpc *Phc2*$^{-/-}$ (A, C, E, G, I, and K) and wild-type (B, D, F, H, J, and L) embryos. The expressions of *Hoxb3* (A and B), *Hoxb4* (C and D), *Hoxb6* (E and F), *Hoxc6* (G and H), *Hoxd4* (I and J), and *Hoxa5* (K and L) are shown. Several prevertebrae are numbered in each panel, and dotted lines indicate the segment boundaries. The arrows indicate anterior boundaries of Hox gene expression.

ical association of Phc2 proteins with the gene (Fig. 5D). We compared the Phc2 association with the first and the second exonic regions of the *p16* gene between the wild-type and Phc2-null MEFs (20). Anti-Phc2 immunoprecipitated a significant quantity of these genomic regions from the wild-type MEFs, but not from *Phc2*$^{-/-}$ MEFs. Therefore, it is likely that Phc2 regulates the transcription of *Cdkn2a* through a direct association with the chromatin.

Synergistic action of *Phc2* with *Phc1* and *Rnf110* mutations. Genetic interactions of mammalian *PcG* mutations have been reported previously using mice that were doubly deficient for either homologous (*Rnf110-Bmi1*) or nonhomologous (*Bmi1-M33* and *Rnf110-Rnf2*) PcG genes (3, 6, 40). The expression of *Hox* genes was synergistically affected in *Rnf110-Bmi1* and *Bmi1-M33* double homozygotes, with the *Rnf110-Bmi1* interaction much stronger in terms of *Hox* derepression. Together with the biochemical evidence, these observations were interpreted as follows. First, the Rnf110, Bmi1, M33, and Rnf2 proteins act in synergy to repress *Hox* genes by forming multimeric protein complexes. Second, homologous PcG gene products have overlapping functions and, to a certain extent, act in a mutually compensatory fashion, as expected from the *Rnf110-Bmi1* double-mutant phenotypes. However, the mutant interactions of a mammalian *ph* homologue with either homologous or nonhomologous PcG genes have not been addressed. Therefore, in this study we generated *Phc2-Phc1* and *Phc2-Rnf110* double homozygotes in order to investigate their axial phenotypes. In particular, it was of interest to compare the impact of *Phc2-Phc1* double deficiency on axial development with that of *Rnf110-Bmi1*, because Phc3, a product of the evolutionarily conserved third *ph* homologue involved in hPRC-H, is still present in the *Phc2-Phc1* double mutants, while the inclusion of an additional Psc homologue has not been reported (27, 44). A comparison of the *Phc2-Phc1* and *Phc2-Rnf110* doubly deficient phenotypes might also allow us to evaluate the functional differences between homologous and nonhomologous interactions among the complexes.

Phc2-Phc1 compound heterozygotes, which were viable, fertile, and externally normal but which exhibited posterior transformations with full penetrance, were intercrossed to produce various compound mutants (Fig. 3C). As expected from the gestational and perinatal lethality of *Phc1* homozygotes, no living *Phc1*$^{-/-}$ pups were found, irrespective of *Phc2* genotypes at birth (41). Importantly, *Phc2*$^{-/-}$-*Phc1*$^{+/-}$ fetuses were alive at 17.5 dpc but did not survive birth, while *Phc2*$^{-/-}$ single mutants were viable (Table 1). Therefore, the heterozygous loss of the *Phc1* gene was shown to affect the survival of *Phc2* homozygotes during the perinatal period. *Phc2*$^{-/-}$-*Phc1*$^{-/-}$

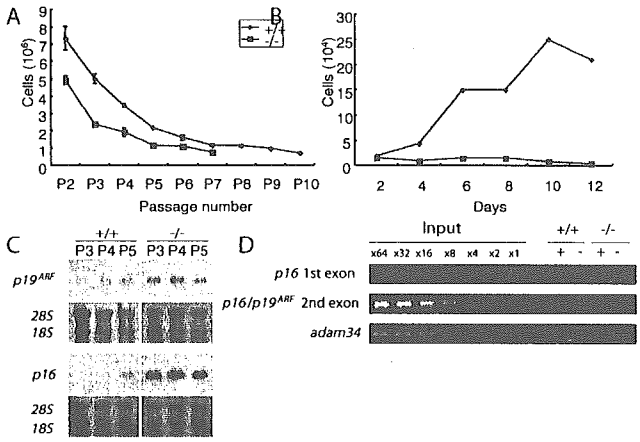

FIG. 5. Defects in the proliferation of *Phc2*$^{-/-}$ MEFs. (A) Cell proliferation using a 3T9 protocol. At 3-day intervals, the total numbers of wild-type and *Phc2*$^{-/-}$ MEFs per culture were determined. The error bars indicate standard errors of the mean. (B) Proliferation of MEFs from respective genotypes at passage 5. (C) Northern analysis of *p16* and *p19*^{ARF} transcripts in wild-type and *Phc2*$^{-/-}$ MEFs at passages 3, 4, and 5 (P3, P4, and P5). The same gel was stained with ethidium bromide to verify the loaded amounts. (D) Distribution of Phc2 proteins in the *Cdkn2a* genomic region in MEFs. Representative results show the association of the Phc2 protein with the second exonic region of *Cdkn2a*, using the *adam34* coding region as a negative control. Immunoprecipitation of the chromatin was performed using the anti-Phc2 antibody (+); mock immunoprecipitation (−) was used as a negative control. Equivalent amounts of genomic DNA from different sources were adjusted and designated ×1.

embryos were lost in a progressive fashion, at an earlier gestational stage than *Phc2*$^{+/+}$-*Phc1*$^{-/-}$, *Phc2*$^{+/-}$-*Phc1*$^{-/-}$, or *Phc2*$^{-/-}$-*Phc1*$^{+/-}$ fetuses, which survived at least until 17.5 dpc (Table 1). These results suggested that *Phc1* and *Phc2* mutations were synergistically affecting the survival of embryos in a gene dosage-dependent manner.

Next, we compared the axial skeletal development of single and compound mutants. Axial skeletal alterations in *Phc2* mutants were similar to but slightly milder than those seen in *Phc1* mutants (Fig. 3A, B, and C); the most prominent differences were seen in the skull. The formation of an ectopic arch associated with the occipital bones, a cleft in the secondary palate, lack of ossification at the center of the presphenoid, and a partial split of the sphenoid bone were seen exclusively in *Phc1*-deficient mice, while changes to the vertebral column were similar in both mutant types. Importantly, skeletal defects due to the respective mutations were exaggerated by the heterozygous mutual loss of another gene. In *Phc2*$^{-/-}$-*Phc1*$^{+/-}$ mice, we observed floating of the dorsal part of the occipital bones, a cleft in the secondary palate, association of anterior processes with C5, detachment of the sixth ribs from the sternum, and a hole in the scapula. These changes were never seen in either *Phc1* single heterozygotes or *Phc2* single homozygotes (Fig. 3A, B, and C). The same was true for *Phc2*$^{+/-}$-*Phc1*$^{-/-}$ mice. Skeletal defects in the vertebral column and scapula were very similar to those seen in *Phc2*$^{-/-}$-*Phc1*$^{+/-}$ mice, including an association of anterior processes with C5, association of imperfect ribs with C6, detachment of the sixth ribs from the sternum, and a hole in the scapula. Defects in the skull were also exaggerated compared to the *Phc1* single mutant, as demonstrated by the obvious segmentation of the exoccipital bone and complete lack of the presphenoid and of the caudal half of the tympanic bone (Fig. 3A, B, and C). Therefore, it appears that homeotic transformations in the axial skeleton and defects in the skull and scapula were synergistically enhanced by *Phc1* and *Phc2* mutations.

Most of the *Phc2*$^{-/-}$-*Phc1*$^{-/-}$ embryos were lost before the mid-gestational stage (Table 1). *Phc2*$^{-/-}$-*Phc1*$^{-/-}$ embryos developed normally up to 8.5 dpc, but severe growth retardation and external abnormalities became progressively evident, and the embryos died from 9.5 dpc onwards. At 9.5 dpc, double-homozygous embryos could be distinguished from their littermates with other genotypes based solely on their size and external morphological features. Internally, further phenotypic distinctions could be made. In the cranial region, the first and second branchial arches were poorly developed. In the trunk and caudal regions, the somitic mesoderm was irregularly segmented; on average, approximately 20 somites were formed in double homozygotes while there were 25 in littermates with other genotypes, and the tail bud was shrunken. Therefore, axial elongation was progressively affected in *Phc2*$^{-/-}$-*Phc1*$^{-/-}$ embryos. These phenotypes were very similar to those seen in *Rnf110-Bmi1* doubly homozygous mice (3).

Because of the early lethality of *Phc2*$^{-/-}$-*Phc1*$^{-/-}$ embryos, we examined the expression of *Hox* cluster genes at 9.5 dpc instead of skeletal development. The anterior boundaries of *Hoxb4* and *-b8* in single mutants were not shifted to any great extent in either of the single mutants compared with the wild type (Fig. 6A). In double homozygotes, *Hoxb4* expression was slightly but significantly derepressed in the cranial region, while the transcription level in the expression domain was not changed (Fig. 6A, a to d). *Hoxb8* expression was not only derepressed in the cranial region but also decreased in its expression domain (Fig. 6A, a to h and hí). Therefore, Phc2 gene products were shown to act in synergy to repress the expression of *Hoxb4* and *-b8* rostral to the expression domain and also to maintain *Hoxb8* expression within its expression domain. Very similar changes have been reported in the *Rnf110-Bmi1* double mutant (12). In addition, since the derepression of *Hoxb6* in *Rnf110-Bmi1* double homozygotes has been shown to occur progressively between 8.5 and 9.5 dpc (3),

TABLE 1. Offspring generated by crossing between *Phc2-Phc1* compound heterozygotes

Phc2-Phc1 genotype	No. (%) of offspring			
	9.5 dpc (n = 283)	10.5 dpc (n = 89)	11.5 dpc (n = 63)	17.5 dpc (n = 63)
+/+ +/+	19 (6.7)	5 (5.6)	6 (9.5)	2 (3.2)
+/+ +/−	38 (13.4)	11 (12.4)	7 (11.1)	10 (15.9)
+/+ −/−	27 (9.5)	3 (3.4)	2 (3.2)	2 (3.2)
+/− +/+	38 (13.4)	11 (12.4)	11 (17.5)	14 (22.2)
+/− +/−	31 (11.0)	8 (9.0)	7 (11.1)	4 (6.4)
+/− −/−	36 (12.7)	10 (11.2)	8 (12.7)	8 (12.7)
−/− +/+	12 (4.2)	6 (6.7)	2 (3.2)	4 (6.4)
−/− +/−	65 (23.0)	24 (27.0)	18 (28.6)	19 (30.2)
−/− −/−	13 (4.6)	7 (7.9)[a]	2 (3.2)[b]	0 (0.0)
ND[c]	4 (1.4)	4 (4.5)	0 (0.0)	0 (0.0)

[a] Two out of seven had no heartbeat.
[b] One out of two was absorbed.
[c] ND, not determined.

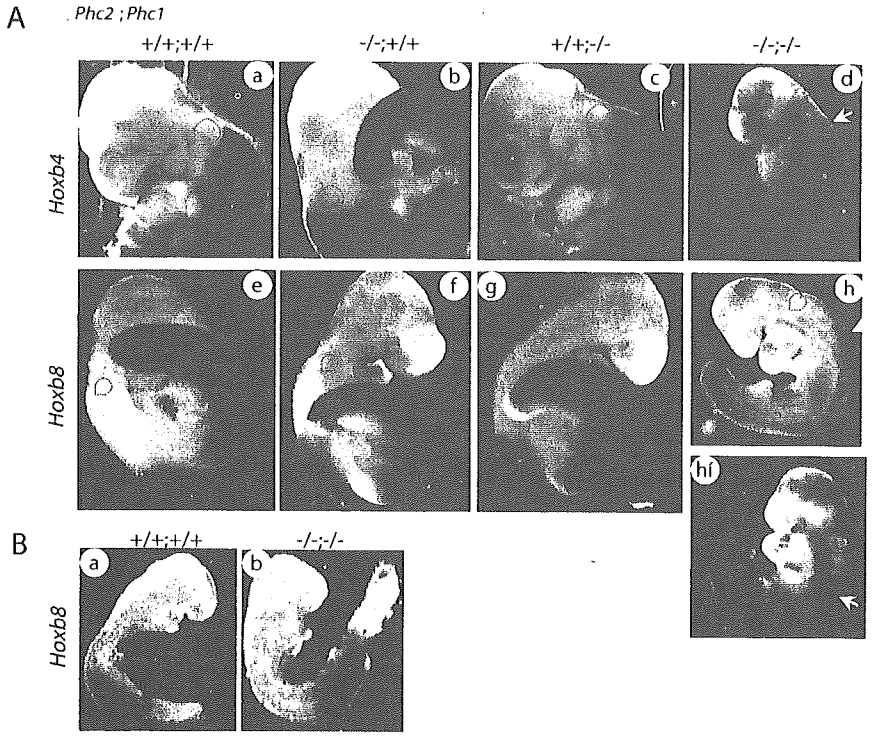

FIG. 6. Expression of *Hoxb4* and *Hoxb8*. (A) *Hoxb4* (frames a to d) and *Hoxb8* (frames e to h) expression in 9.5-dpc wild-type and *Phc2* and *Phc1* single homozygotes and double homozygotes; the genotypes are indicated across the top. Each specimen was subjected to chromogenic reaction for the same length of time. The specimen shown in frame h was subjected to a longer chromogenic reaction (frame hí). Dotted lines indicate the otic vesicles in this series of figures. The prospective anterior boundary of the expression is indicated by a yellow arrow in double homozygotes. All pictures for both *Hoxb4* and *Hoxb8* expressions were taken under the same magnification. (B) *Hoxb8* expression in 8.5-dpc wild-type and double-homozygous embryos; the pictures were taken under the same magnification.

we also looked at *Hoxb8* expression at the earlier gestational time point of 8.5 dpc. In our study, *Hoxb8* expression was not significantly altered in the 8.5-dpc embryos (Fig. 6B). Therefore, based on these results, it appears that Phc1 and Phc2 are involved in maintaining the transcriptional status of *Hoxb8* rather than in its early induction, as observed in *Rnf110-Bmi1* double homozygotes (3, 12).

Following this, we looked at the genetic interactions between the *Phc2* and *Rnf110* mutations. Since $Phc2^{-/-}$-$Rnf110^{+/-}$ mice were viable and fertile, they were intercrossed to generate double homozygotes. $Phc2^{-/-}$-$Rnf110^{-/-}$ mice died during late gestation, around 18.5 dpc, while most *Phc2* and *Rnf110* single mutants were shown to grow to adulthood (1). Furthermore, skeletal defects in double homozygotes were stronger than in either of the respective single mutants and resembled those in $Phc2^{+/-}$-$Phc1^{-/-}$ and $Phc2^{-/-}$-$Phc1^{+/-}$ mice (Fig. 7). Several defects were observed: the occipital bones were clearly segmented to form an ectopic arch, while the basioccipital bone was not completely segmented; the middle parts of the skull base and scapula failed to undergo cartilaginous condensation; the upper horn of the hyoid bone was fused to the styloid process; and the entire rib cage was shifted anteriorly more perfectly than in either respective single mutant. Unlike the *Phc2-Phc1* interactions, the skeletal phenotypes of the respective single homozygotes were not exaggerated by the heterozygous mutual loss of another gene (Shinga and Koseki, unpublished). Taken together, these results showed that the *Phc2* mutation affected the survival and A-P patterning of the axial skeleton in synergy with the *Rnf110* mutation, but to a lesser degree than was observed with the *Phc1* mutation.

Direct association of Phc2 with the *Hoxb8* locus. The significant impacts of the *Phc2* mutation on the transcriptional regulation of *Hox* genes prompted us to investigate the physical association of Phc2 proteins with the *Hoxb8* locus using ChIP (Fig. 8A). We dissected 11.5-dpc embryos into cranial and caudal parts, in which the transcription of *Hoxb8* transcription is silent and active, respectively. Phc2 association was examined at the upstream enhancer (BH1100 region), putative promoter region, and first exon of *Hoxb8* and the upstream enhancer region of *Hoxb7* (KA region) (9). Phc2 was associated with these genomic regions irrespective of transcriptional status, as was the case with Phc1 (Fig. 8B). Therefore, it is likely that Phc2 and Phc1 regulate the transcription of *Hoxb8* through a direct association with the chromatin.

Analysis of the comparative expression of Phc2 and Phc1 in various tissues. Although genetic evidence suggests that Phc2 and Phc1 gene products act in a redundant manner, it is also true that the single deficient phenotypes for *Phc2* and *Phc1* are not identical. In particular, overt defects in the hematopoietic lineage or cranial neural crest derivatives are seen exclusively in *Phc1* mutants (41, 43). Importantly, *Phc2* and *Rnf110* mutations synergistically affect the proliferation of interleukin 7 receptor α-positive lymphoid precursor cells residing in the

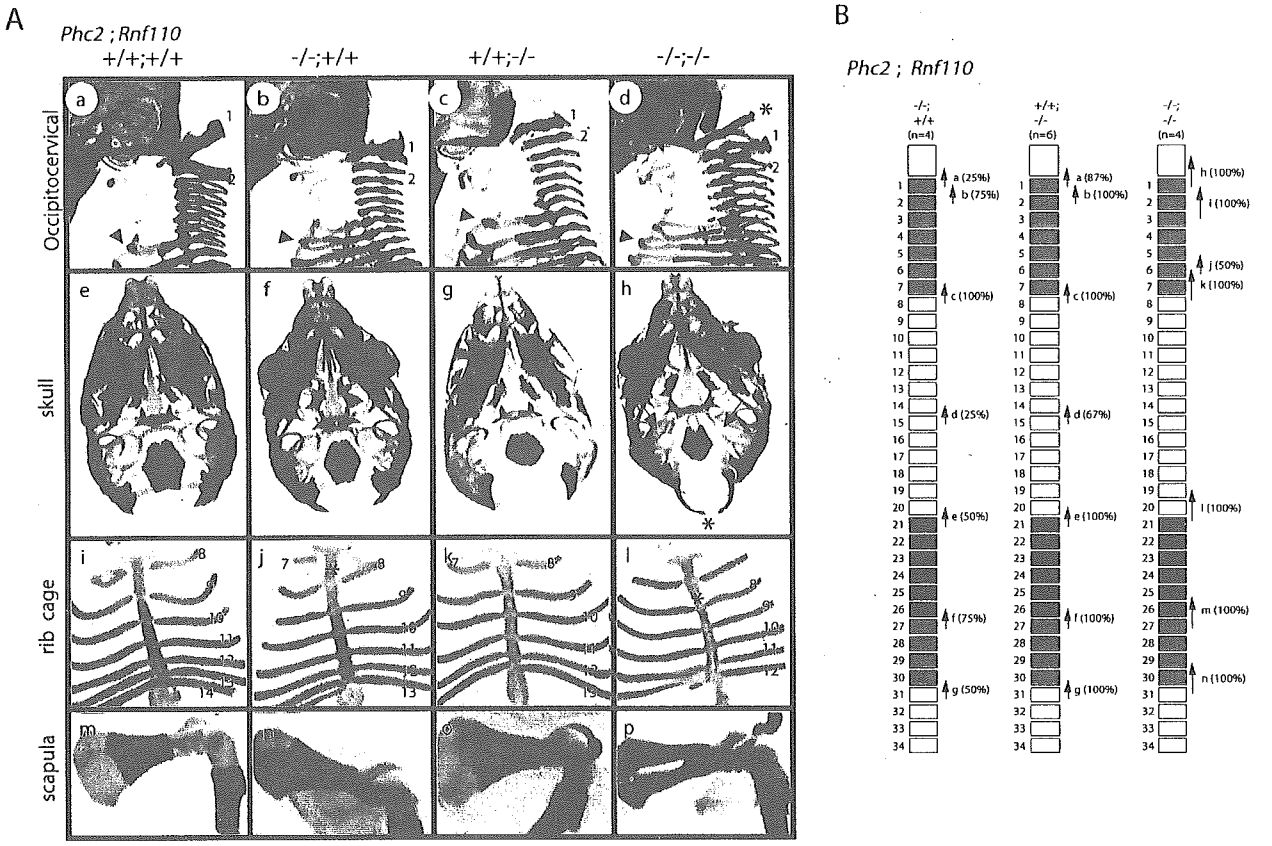

FIG. 7. Gene dose-dependent skeletal alterations in wild-type and *Phc2* and *Rnf110* single homozygotes and double homozygotes. (A) The genotypes of the specimens are shown along the top of the frames. (Frames a to d) Lateral views of the occipitocervical region. The arrowheads indicate the ribs associated with the eighth vertebrae. C1 and C2 are indicated numerically, and asterisks indicate the ectopic arch or piece. (Frames d and h) An asterisk indicates an ectopic arch that represents perfect segmentation of the exoccipital bone. Red arrows indicate ectopic cartilaginous condensation bridging the hyoid bone and styloid process, while the dotted line indicates the lack of cartilaginous condensation between the occipital and sphenoid bones. (Frames e to h) Ventral views of the skull. (Frames i to l) Ventral views of rib cages. The numbers of vertebrae to which ribs are attached are indicated numerically. Asterisks indicate the sternums that are shifted anteriorly in *Phc2* single (frame j) and double (frame l) homozygotes. (Frames m to p) Overviews of the scapula. (B) Summary of posterior transformations: (a) supraoccipital bone→C1, appearance of the ectopic arch or bone; (b) C1→C2, fusion of the odontoid process to the C1 vertebra; (c) C7→T1, association of the cervical rib with C7; (d) T7→T8, dissociation of the seventh rib from the sternum; (e) T13→L1, loss of the rib from the 20th vertebra; (f) L6→S1, formation of a sacroiliac joint in the 26th vertebra; (g) S4→Ca1, appearance of the first caudal vertebra in the 30th vertebra; (h) more perfect supraoccipital bone→C1 transformation, perfect segmentation of supra- and exoccipital bones; (i) C1→C3, overall structure similar to C3 rather than C2; (j) C5→C6, association of the anterior tuberculus with the C5 vertebra; (k) C6→T1, association of the cervical rib with C6; (l) T12→L1, loss of the rib from the 19th vertebra; (m) L4→S1, formation of a sacroiliac joint in the 25th vertebra; (n) S3→Ca1, appearance of the first caudal vertebra in the 29th vertebra.

fetal gut, while single mutants are unaffected (T. Sato and H. Koseki, submitted for publication). This implies that the involvement of Phc2 during the proliferation of lymphoid precursors is dispensable and that latent defects in hematopoietic lineage development might presumably be fully compensated for by Phc1 and/or Phc3 in Phc2-deficient mice. It has therefore been suggested that the phenotypical differences between *Phc2* and *Phc1* single mutants might be attributable to tissue- and/or stage-specific variations in their expression or requirement (17). To address this issue, we compared the expression of *Phc2* and *Phc1* in various tissues by RT-PCR (Fig. 9A). *Phc2* transcripts were detected as 383-bp PCR products and *Phc1* as at least 346 and 502 bp due to the differential usage of exons. The expression of *Phc2* and *Phc1* was seen in all the tissues examined, although the levels varied. Tissue-specific variation of expression was noticeably more prominent in *Phc1* than *Phc2*.

We extended our analysis to lymphocyte subpopulations in bone marrow, thymus, naïve and immunized spleen, and B lymphocytes activated by various signals, since the role of Phc2 was shown to be dispensable (Fig. 9B). Developing B and T lymphocytes in the bone marrow and thymus, respectively, and B-cell subpopulations in naïve and immunized spleens, were fractionated according to their developmental stages. *Phc2* and *Phc1* expression was seen in all fractions, and while *Phc1* expression was variable, that of Phc2 was not. This developmental-stage-specific variation in *Phc1* expression prompted us to examine whether the expression of *Phc2* and *Phc1* in resting B lymphocytes was regulated by various inductive signals mediated by B-cell receptor cross-linking, B-cell activation factor

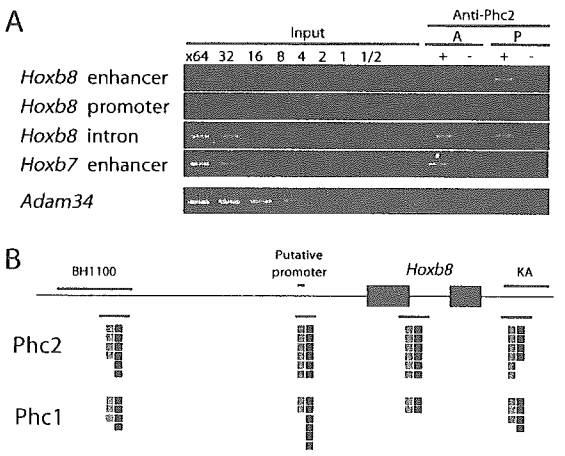

FIG. 8. Distribution of Phc2 proteins in the *Hoxb8* genomic region at 11.5 dpc. (A) Representative results showing the association of the Phc2 protein with the *Hoxb8* enhancer and promoter and intronic and *Hoxb7* enhancer regions, with the *adam34* coding region as a negative control. The positions of PCR fragments are shown in panel B. Tissues of 12.5-dpc embryos were dissected, and chromatin fractions were purified from transcriptionally silent anterior (A) and active posterior (P) tissues (mesoderm plus neurectoderm). Immunoprecipitation of the chromatin was performed by the anti-Phc2 antibody (+); mock immunoprecipitation (−) was used as a negative control. Equivalent amounts of genomic DNAs from different sources were adjusted and designated 1′. (B) The distribution of Phc2 in the *Hoxb8* genomic region is schematically represented. The black and gray squares represent the degree of enrichment of immunoprecipitated genomic DNA in posterior and anterior tissues, respectively: each square represents a twofold enrichment in comparison with the unfractionated "input" DNA. The distribution of Phc1 is shown as a reference.

from the TNF family (BAFF) stimulation, CD40 ligation, or lipopolysaccharide (LPS) stimulation (Fig. 9C). The engagement of B-cell receptor by anti-IgM antibodies induces the survival and cell cycle entry of resting B cells (24); BAFF functions to maintain B-cell viability but does not induce S-phase entry of the cell cycle (28); CD40 ligation by anti-CD40 induces the survival, cell cycle progression, and up-regulation of a variety of adhesion molecules for cell-cell interaction (7); and LPS represents a T-independent antigen that has potent mitogenic activity on B cells (30). Interestingly, these signals significantly increased *Phc1* expression within 1 hour, whereas they had no effect on *Phc2*. Up-regulation of *Phc1* expression induced by BAFF persisted for at least 7 h, while induction by other signals was transient. Therefore, Phc1 expression appears to be regulated by various inductive stimuli, whereas Phc2 is expressed in a constitutive manner.

DISCUSSION

In this study, we have provided biochemical and genetic evidence to indicate that Phc2 is a functional component of class II PcG complexes during embryogenesis. Phc2 is constitutively involved in an hPRC-H-like complex with other constituents of class II PcG complexes and associates with the *Hoxb8* genomic regions at 11.5 dpc. We have shown that the *Phc2* mutant allele is involved in the mediation of the transcriptional repression of the *Hox* cluster genes in mid-gestational embryos and the *Cdkn2a* genes in MEFs; similar findings have been reported for other mammalian *PcG* mutants. The synergistic actions of the *Phc2* mutation with the *Phc1* and *Rnf110* mutations during A-P specification demonstrate that *Hox* repression by Phc2 is mediated through the class II PcG complexes. *Phc2-Phc1* double deficiency reveals that Phc2 and Phc1 act synergistically to maintain the repression of *Hox* genes but are not involved in early induction.

The genetic evidence provided by this study allows us to evaluate further the functional complicity of Phc2 with Phc1 in vivo. Although both Phc1 and Rnf110 associate and form complexes with Phc2, the *Phc1* mutation exacerbated the *Phc2* mutant phenotypes to a much greater extent than the *Rnf110* mutation in terms of *Hox* derepression and embryonic survival. These different modes of genetic interaction are at least partly due to functional overlap and the mutually compensatory properties of Phc2 with Phc1, but not with Rnf110. Indeed, in vitro pull-down and yeast two-hybrid assays have shown that Phc2 and Phc1 interact with almost the same set of PcG proteins and that the primary structures of their functional domains are highly conserved (16, 18, 25, 36). This is also consistent with in vitro evidence that the inhibition of remodeling and transcription, and the recruitment of a free polynucleosomal array mediated by hPRC-H and PRC1 in the solution, is mostly substituted by mouse PRC core complexes (mPCCs) comprised exclusively of Phc1, M33, Rnf2, and either Rnf110 or Bmi1, although the original hPRC-H harbors Phc1, Phc2, and Phc3 (26, 27). Nevertheless, it is also true that the single deficient phenotypes for *Phc2* and *Phc1* are not identical. These phenotypical differences between *Phc2* and *Phc1* single mutants might be at least partly attributed to tissue- and/or stage-specific variations in their expression or requirement (17), a concept that is supported by the results of the comparative expression analyses of *Phc2* and *Phc1* in this study. Although Phc2 and Phc1 act in a highly compensatory manner, both mutants still exhibit very similar derepression of *Hox* cluster genes. This leads us to hypothesize that the overall quantity of *ph* orthologues in the nuclei may also be an important parameter for class II PcG complexes, allowing them to exert their molecular functions, at least at the *Hox* loci, as well as Psc orthologues (3). We were able to show by using ChIP that Phc2 and Phc1 consistently associate together with several *Hoxb8* genomic regions. Furthermore, a strict dose-dependent requirement for Phc2 and Phc1 is seen during A-P specification of the axis.

Biochemical analyses suggest that the ability of mPCC to inhibit remodeling and transcription, as well as to bridge chromatin templates, might represent substantially separate functions requiring different subunits (26). While Phc1 plays a key role in bridging chromatin templates in vitro, it is dispensable for binding to a chromatin template and inhibiting its remodeling. *Phc2-Phc1* double homozygotes reveal that the molecular processes mediated by Phc2 and Phc1 are essential for the maintenance of *Hox* repression by class II PcG complexes. The recruitment activity is expected to represent a long-range interaction or spreading of class II PcG complexes on the genome, which is likely to be mediated through interactions among PcG proteins. Therefore, class II PcG complexes that lack both Phc2 and Phc1 may fail to mediate PcG repression because of defects in long-range effects. The oligomerization of PcG complexes, mediated by heterotypic and/or homotypic

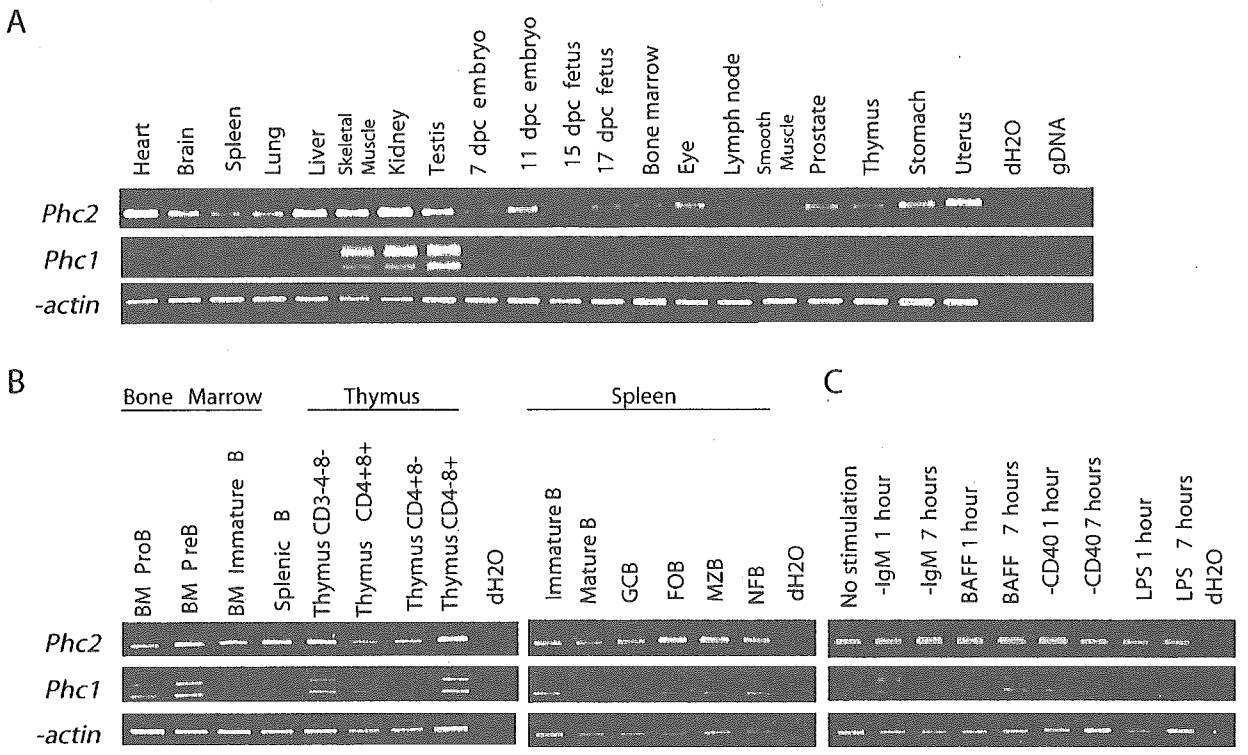

FIG. 9. The expression of *Phc2* and *Phc1* in various tissues, lymphocyte subpopulations, and B lymphocytes induced by various extracellular stimuli. (A) The expression of *Phc2* and *Phc1* was examined by reverse transcriptase-PCR in various adult tissues and whole embryos at 7, 11, 15, and 17 days postcoitus. Distilled water (dH_2O) and mouse genomic DNA (gDNA) were used as negative controls; β-*actin* was used to normalize the amounts of cDNA. (B) The expression of *Phc2* and *Phc1* was examined in developing B and T lymphocytes in the bone marrow and thymus, respectively, and B-cell subpopulations in naïve and immunized spleens. Mature splenic B cells were fractionated into germ center B (GCB), follicular B (FOB), marginal zone B (MZB), and newly formed B (NFB) subpopulations. *Phc2* did not exhibit any variation in expression levels, in contrast to *Phc1*, where the level of expression was variable. (C) Expression of *Phc2* and *Phc1* in resting B lymphocytes upon activation by B-cell receptor engagement by α-IgM, BAFF stimulation, CD40 ligation by α-CD40, and LPS stimulation.

interactions of the SAM domains of Phc2 and Phc1, plays a key role because the self-association activity of the SAM domain of SCM has been shown to be closely correlated with PcG repression in *Drosophila* (37). Given that mPCC-like complexes act as a fundamental unit of class II PcG complexes in vivo, oligomerization of mPCC-like complexes via the SAM domains of *ph* orthologues may be an essential process in the formation of functional class II PcG complexes on the chromatin (26, 36, 43). Consistent with this is the close association of Phc2 with Phc1, as demonstrated by both co-IP and ChIP analyses in our study and elsewhere (16). Interestingly, Phc3 remains present in *Phc2-Phc1* double mutants, while the inclusion of an additional Psc homologue has not been reported in class II PcG complexes, although the double-mutant phenotypes for *Phc2-Phc1* and *Rnf110-Bmi1* are almost identical (3, 27, 44). This implies that Phc3 alone may not be quantitatively sufficient to allow the oligomerization of PcG complexes, or possibly excess amount of mPCCΔPhc2- or mPCCΔPhc1-like complexes may affect the oligomerization of mPCC-like complexes containing Phc3.

In this study, we also showed that both Phc2 and Phc1 gene products associate with the *Hoxb8* genomic region within the transcriptionally active domain, as well as within the repressed loci. This finding is consistent with previous reports that the predominant subnuclear localization of several PcG proteins is in the perichromatin compartment, where most pre-mRNA synthesis takes place (10). It is possible that these results tie in with the recent discovery that class II PcG complexes are associated with a positive function. Null mutations in the *Rnf110* and *Phc1* loci have been shown to decrease the transcription level of endogenous *Hoxb1* and to severely impair the transcription from *Hox-LacZ* reporters and knockin loci (12). In addition, a positive action of PcG complexes could explain the fall in gene expression levels within *Hoxb8* expression domains, which has been reported to be around 9.5 dpc in *Phc2-Phc1* and *Bmi1-Rnf110* and double mutants (3, 12). Importantly, the transcriptional silencing of *Hox*-reporter loci in *Rnf110* and *Phc1* mutants is accompanied by DNA methylation of the promoter region (12). Therefore, the positive role of class II PcG gene products, mediated by their physical association with *Hoxb8* genomic regions, may involve local suppression of the pathway leading to local DNA methylation. However, it is still conceivable that the PcG gene products act by repressing the expression of *Hox* transcription repressors. This possibility needs to be addressed in the future.

ACKNOWLEDGMENTS

This project was supported by Special Coordination Funds for the Promotion of Science and Technology from the Ministry of Education,

Culture, Sports, Science and Technology of the Japanese Government (H.K.).

This paper is dedicated to the memory of Shozo Sugimori, who was responsible for the care of the mutant animals used in this study. We are also grateful to T. Hasegawa and to M. Iida, M. Uchida, and R Moriizumi for their help.

REFERENCES

1. **Akasaka, T., M. Kanno, R. Balling, M. A. Mieza, M. Taniguchi, and H. Koseki.** 1996. A role for mel-18, a Polycomb group-related vertebrate gene, during the anteroposterior specification of the axial skeleton. Development **122:**1513–1522.
2. **Akasaka, T., K. Tsuji, H. Kawahira, M. Kanno, K. Harigaya, L. Hu, Y. Ebihara, T. Nakahata, O. Tetsu, M. Taniguchi, and H. Koseki.** 1997. The role of mel-18, a mammalian Polycomb group gene, during IL-7-dependent proliferation of lymphocyte precursors. Immunity **7:**135–146.
3. **Akasaka, T., M. van Lohuizen, N. van der Lugt, Y. Mizutani-Koseki, M. Kanno, M. Taniguchi, M. Vidal, M. Alkema, A. Berns, and H. Koseki.** 2001. Mice doubly deficient for the Polycomb Group genes Mel18 and Bmi1 reveal synergy and requirement for maintenance but not initiation of Hox gene expression. Development **128:**1587–1597.
4. **Alkema, M. J., M. Bronk, E. Verhoeven, A. Otte, L. J. van 't Veer, A. Berns, and M. van Lohuizen.** 1997. Identification of Bmi1-interacting proteins as constituents of a multimeric mammalian polycomb complex. Genes Dev. **11:**226–240.
5. **Atsuta, T., Y. Fujimura, H. Moriya, M. Vidal, T. Akasaka, and H. Koseki.** 2001. Production of monoclonal antibodies against mammalian Ring1B proteins. Hybridoma **20:**43–46.
6. **Bel, S., N. Core, M. Djabali, K. Kieboom, N. van der Lugt, M. J. Alkema, and M. van Lohuizen.** 1998. Genetic interactions and dosage effects of Polycomb group genes in mice. Development **125:**3543–3551.
7. **Bishop, G. A., and B. S. Hostager.** 2003. The CD40-CD154 interaction in B cell-T cell liaisons. Cytokine Growth Factor Rev. **14:**297–309.
8. **Bornemann, D., E. Miller, and J. Simon.** 1996. The Drosophila Polycomb group gene Sex comb on midleg (Scm) encodes a zinc finger protein with similarity to polyhomeotic protein. Development **122:**1621–1630.
9. **Charite, J., W. de Graaff, R. Vogels, F. Meijlink, and J. Deschamps.** 1995. Regulation of the Hoxb-8 gene: synergism between multimerized cis-acting elements increases responsiveness to positional information. Dev. Biol. **171:** 294–305.
10. **Cmarko, D., P. J. Verschure, A. P. Otte, R. van Driel, and S. Fakan.** 2003. Polycomb group gene silencing proteins are concentrated in the perichromatin compartment of the mammalian nucleus. J. Cell Sci. **116:**335–343.
11. **Core, N., S. Bel, S. J. Gaunt, M. Aurrand-Lions, J. Pearce, A. Fisher, and M. Djabali.** 1997. Altered cellular proliferation and mesoderm patterning in Polycomb-M33-deficient mice. Development **124:**721–729.
12. **de Graaff, W., D. Tomotsune, T. Oosterveen, Y. Takihara, H. Koseki, and J. Deschamps.** 2003. Randomly inserted and targeted Hox/reporter fusions transcriptionally silenced in Polycomb mutants. Proc. Natl. Acad. Sci. USA **100:**13362–13367.
13. **del Mar Lorente, M., C. Marcos-Gutierrez, C. Perez, J. Schoorlemmer, A. Ramirez, T. Magin, and M. Vidal.** 2000. Loss- and gain-of-function mutations show a polycomb group function for Ring1A in mice. Development **127:**5093–5100.
14. **Dura, J. M., N. B. Randsholt, J. Deatrick, I. Erk, P. Santamaria, J. D. Freeman, S. J. Freeman, D. Weddell, and H. W. Brock.** 1987. A complex genetic locus, polyhomeotic, is required for segmental specification and epidermal development in D. melanogaster. Cell **51:**829–839.
15. **Franke, A., M. DeCamillis, D. Zink, N. Cheng, H. W. Brock, and R. Paro.** 1992. Polycomb and polyhomeotic are constituents of a multimeric protein complex in chromatin of *Drosophila melanogaster*. EMBO J. **11:**2941–2950.
16. **Gunster, M. J., D. P. Satijn, K. M. Hamer, J. L. den Blaauwen, D. de Bruijn, M. J. Alkema, M. van Lohuizen, R. van Driel, and A. P. Otte.** 1997. Identification and characterization of interactions between the vertebrate polycomb-group protein BMI1 and human homologs of polyhomeotic. Mol. Cell. Biol. **17:**2326–2335.
17. **Gunster, M. J., F. M. Raaphorst, K. M. Hamer, J. L. den Blaauwen, E. Fieret, C. J. Meijer, and A. P. Otte.** 2001. Differential expression of human Polycomb group proteins in various tissues and cell types. J. Cell Biochem. **81:**129–143.
18. **Hemenway, C. S., B. W. Halligan, and L. S. Levy.** 1998. The Bmi-1 oncoprotein interacts with dinG and MPh2: the role of RING finger domains. Oncogene **16:**2541–2547.
19. **Jacobs, J. J., K. Kieboom, S. Marino, R. A. DePinho, and M. van Lohuizen.** 1999. The oncogene and Polycomb-group gene bmi-1 regulates cell proliferation and senescence through the ink4a locus. Nature **397:**164–168.
20. **Kamijo, T., F. Zindy, M. F. Roussel, D. E. Quelle, J. R. Downing, R. A. Ashmun, G. Grosveld, and C. J. Sherr.** 1997. Tumor suppression at the mouse INK4a locus mediated by the alternative reading frame product p19ARF. Cell **91:**649–659.
21. **Katoh-Fukui, Y., R. Tsuchiya, T. Shiroishi, Y. Nakahara, N. Hashimoto, K. Noguchi, and T. Higashinakagawa.** 1998. Male-to-female sex reversal in M33 mutant mice. Nature **393:**688–692.
22. **Kessel, M., and P. Gruss.** 1991. Homeotic transformations of murine vertebrae and concomitant alteration of Hox codes induced by retinoic acid. Cell **67:**89–104.
23. **Kim, C. A., M. Gingery, R. M. Pilpa, and J. U. Bowie.** 2002. The SAM domain of polyhomeotic forms a helical polymer. Nat. Struct. Biol. **9:**453–457.
24. **Kraus, M., M. B. Alimzhanov, N. Rajewsky, and K. Rajewsky.** 2004. Survival of resting mature B lymphocytes depends on BCR signaling via the Igα β heterodimer. Cell **117:**787–800.
25. **Kyba, M., and H. W. Brock.** 1998. The SAM domain of polyhomeotic, RAE28, and scm mediates specific interactions through conserved residues. Dev. Genet. **22:**74–84.
26. **Lavigne, M., N. J. Francis, I. F. King, and R. E. Kingston.** 2004. Propagation of silencing; recruitment and repression of naive chromatin in trans by polycomb repressed chromatin. Mol. Cell. **13:**415–425.
27. **Levine, S. S., A. Weiss, H. Erdjument-Bromage, Z. Shao, P. Tempst, and R. E. Kingston.** 2002. The core of the polycomb repressive complex is compositionally and functionally conserved in flies and humans. Mol. Cell. Biol. **22:**6070–6078.
28. **Mackay, F., and J. L. Browning.** 2002. BAFF: a fundamental survival factor for B cells. Nat. Rev. Immunol. **2:**465–475.
29. **Miyagishima, H., K. Isono, Y. Fujimura, M. Iyo, Y. Takihara, H. Masumoto, M. Vidal, and H. Koseki.** 2003. Dissociation of mammalian Polycomb-group proteins, Ring1B and Rae28/Ph1, from the chromatin correlates with configuration changes of the chromatin in mitotic and meiotic prophase. Histochem. Cell Biol. **120:**111–119.
30. **Miyake, K.** 2004. Innate recognition of lipopolysaccharide by Toll-like receptor 4-MD-2. Trends Microbiol. **12:**186–192.
31. **Nagy, A., J. Rossant, R. Nagy, W. Abramow-Newerly, and J. C. Roder.** 1993. Derivation of completely cell culture-derived mice from early-passage embryonic stem cells. Proc. Natl. Acad. Sci. USA **90:**8424–8428.
32. **Nomura, M., Y. Takihara, and K. Shimada.** 1994. Isolation and characterization of retinoic acid-inducible cDNA clones in F9 cells: one of the early inducible clones encodes a novel protein sharing several highly homologous regions with a *Drosophila* polyhomeotic protein. Differentiation **57:**39–50.
33. **Orlando, V., H. Strutt, and R. Paro.** 1997. Analysis of chromatin structure by in vivo formaldehyde cross-linking. Methods **11:**205–214.
34. **Paro, R.** 1995. Propagating memory of transcriptional states. Trends Genet. **11:**295–297.
35. **Peters, A. H., S. Kubicek, K. Mechtler, R. J. O'Sullivan, A. A. Derijck, L. Perez-Burgos, A. Kohlmaier, S. Opravil, M. Tachibana, Y. Shinkai, J. H. Martens, and T. Jenuwein.** 2003. Partitioning and plasticity of repressive histone methylation states in mammalian chromatin. Mol. Cell **12:**1577–1589.
36. **Peterson, A. J., M. Kyba, D. Bornemann, K. Morgan, H. W. Brock, and J. Simon.** 1997. A domain shared by the Polycomb group proteins Scm and ph mediates heterotypic and homotypic interactions. Mol. Cell. Biol. **17:**6683–6692.
37. **Peterson, A. J., D. R. Mallin, N. J. Francis, C. S. Ketel, J. Stamm, R. K. Voeller, R. E. Kingston, and J. A. Simon.** 2004. Requirement for sex comb on midleg protein interactions in *Drosophila* polycomb group repression. Genetics **167:**1225–1239.
38. **Pirrotta, V.** 1997. PcG complexes and chromatin silencing. Curr. Opin. Genet. Dev. **7:**249–258.
39. **Shao, Z., F. Raible, R. Mollaaghababa, J. R. Guyon, C. T. Wu, W. Bender, and R. E. Kingston.** 1999. Stabilization of chromatin structure by PRC1, a Polycomb complex. Cell **98:**37–46.
40. **Suzuki, M., Y. Mizutani-Koseki, Y. Fujimura, H. Miyagishima, T. Kaneko, Y. Takada, T. Akasaka, H. Tanzawa, Y. Takihara, M. Nakano, H. Masumoto, M. Vidal, K. Isono, and H. Koseki.** 2002. Involvement of the Polycomb-group gene Ring1B in the specification of the anterior-posterior axis in mice. Development **129:**4171–4183.
41. **Takihara, Y., D. Tomotsune, M. Shirai, Y. Katoh-Fukui, K. Nishii, M. A. Motaleb, M. Nomura, R. Tsuchiya, Y. Fujita; Y. Shibata, T. Higashinakagawa, and K. Shimada.** 1997. Targeted disruption of the mouse homologue of the *Drosophila* polyhomeotic gene leads to altered anteroposterior patterning and neural crest defects. Development **124:**3673–3682.
42. **Tomotsune, D., Y. Takihara, J. Berger, D. Duhl, S. Joo, M. Kyba, M. Shirai, H. Ohta, Y. Matsuda, B. M. Honda, J. Simon, K. Shimada, H. W. Brock, and F. Randazzo.** 1999. A novel member of murine Polycomb-group proteins, Sex comb on midleg homolog protein, is highly conserved, and interacts with RAE28/mph1 in vitro. Differentiation **65:**229–239.
43. **Tomotsune, D., M. Shirai, Y. Takihara, and K. Shimada.** 2000. Regulation of Hoxb3 expression in the hindbrain and pharyngeal arches by rae28, a member of the mammalian Polycomb group of genes. Mech. Dev. **98:**165–169.
44. **Tonkin, E., D. M. Hagan, W. Li, and T. Strachan.** 2002. Identification and

characterisation of novel mammalian homologues of *Drosophila* polyhomeotic permits new insights into relationships between members of the polyhomeotic family. Hum. Genet. **111**:435–442.

45. **van der Lugt, N. M., J. Domen, K. Linders, M. van Roon, E. Robanus-Maandag, H. te Riele, M. van der Valk, J. Deschamps, M. Sofroniew, M. van Lohuizen, and A. Berns.** 1994. Posterior transformation, neurological abnormalities, and severe hematopoietic defects in mice with a targeted deletion of the bmi-1 proto-oncogene. Genes Dev. **8**:757–769.
46. **van der Vlag, J., and A. P. Otte.** 1999. Transcriptional repression mediated by the human polycomb-group protein EED involves histone deacetylation. Nat. Genet. **23**:474–478.
47. **Voncken, J. W., B. A. Roelen, M. Roefs, S. de Vries, E. Verhoeven, S. Marino, J. Deschamps, and M. van Lohuizen.** 2003. Rnf2 (Ring1b) deficiency causes gastrulation arrest and cell cycle inhibition. Proc. Natl. Acad. Sci. USA **100**:2468–2473.
48. **Wilkinson, D. G., and M. A. Nieto.** 1993. Detection of messenger RNA by in situ hybridization to tissue sections and whole mounts. Methods Enzymol. **225**:361–373.
49. **Yamaki, M., K. Isono, Y. Takada, K. Abe, T. Akasaka, H. Tanzawa, and H. Koseki.** 2002. The mouse Edr2 (Mph2) gene has two forms of mRNA encoding 90- and 36-kDa polypeptides. Gene **288**:103–110.
50. **Zhang, H., A. Christoforou, L. Aravind, S. W. Emmons, S. Van Den Heuvel, and D. A. Haber.** 2004. The *C. elegans* Polycomb gene sop-2 encodes an RNA binding protein. Mol. Cell **14**:841–847.

DNA polymerase θ contributes to the generation of C/G mutations during somatic hypermutation of Ig genes

Keiji Masuda*, Rika Ouchida*, Arata Takeuchi†, Takashi Saito†, Haruhiko Koseki‡, Kiyoko Kawamura§, Masatoshi Tagawa§, Takeshi Tokuhisa¶, Takachika Azuma‖, and Jiyang O-Wang*,**

Laboratories for *Antigen Receptor Diversity, †Cell Signaling, and ‡Developmental Genetics, Research Center for Allergy and Immunology, RIKEN Yokohama Institute, Yokohama, Kanagawa 230-0045, Japan; §Division of Pathology, Chiba Cancer Center Research Institute, Chiba 260-8717, Japan; ¶Department of Developmental Genetics, Graduate School of Medicine, Chiba University, Chiba 260-8670, Japan; and ‖Division of Biosignaling, Research Institute for Biological Science, Tokyo University of Science, Chiba 278-0022, Japan

Edited by Frederick W. Alt, Harvard Medical School, Boston, MA, and approved August 10, 2005 (received for review July 6, 2005)

Somatic hypermutation of Ig variable region genes is initiated by activation-induced cytidine deaminase; however, the activity of multiple DNA polymerases is required to ultimately introduce mutations. DNA polymerase η (Polη) has been implicated in mutations at A/T, but polymerases involved in C/G mutations have not been identified. We have generated mutant mice expressing DNA polymerase (Polθ) specifically devoid of polymerase activity. Compared with WT mice, Polq-inactive (Polq, the gene encoding Polθ) mice exhibited a reduced level of serum IgM and IgG1. The mutant mice mounted relatively normal primary and secondary immune responses to a T-dependent antigen, but the production of high-affinity specific antibodies was partially impaired. Analysis of the J_H4 intronic sequences revealed a slight reduction in the overall mutation frequency in Polq-inactive mice. Remarkably, although mutations at A/T were unaffected, mutations at C/G were significantly decreased, indicating an important, albeit not exclusive, role for Polθ activity. The reduction of C/G mutations was particularly focused on the intrinsic somatic hypermutation hotspots and both transitions and transversions were similarly reduced. These findings, together with the recent observation that Polθ efficiently catalyzes the bypass of abasic sites, lead us to propose that Polθ introduces mutations at C/G by replicating over abasic sites generated via uracil-DNA glycosylase.

abasic site | low-fidelity DNA polymerase | activation-induced cytidine deaminase | uracil-DNA glycosylase

Functional Ig genes are assembled in developing B cells by recombination-activating gene-mediated rearrangement of the germline V, D, and J gene segments (1–3). This process generates a primary repertoire of B cells expressing diversified surface immunoglobulins. Upon antigen stimulation and in the presence of T cell help, B cells undergo further diversification of their Ig genes, namely somatic hypermutation (SHM) and class switch recombination (CSR), in the germinal centers (GCs) of secondary lymphoid organs such as spleen, lymph node, and Peyer's patches (4). Both SHM and CSR are initiated by a single enzyme, activation-induced cytidine deaminase, which catalyzes the deamination of C to U on DNA and/or possibly on an as-yet-hypothetical endonuclease mRNA (5–7). Although the mechanism of SHM is still not fully understood, it is thought that mutations are ultimately introduced by error-prone DNA polymerases during the DNA repair process (7, 8).

Approximately 10 new low-fidelity DNA polymerases have been identified in the past several years (9, 10). DNA polymerase θ (Polθ) is a ≈300-kDa family A polymerase with a unique structure, having a helicase domain in its N-terminal portion and a polymerase domain in its C terminus (11–13). *Polq*, the gene encoding Polθ, has a homolog in *Drosophila*, the *mus308* gene (14). Mutant flies exhibited hypersensitivity to DNA interstrand crosslinking agents such as cisplatinum but not to alkylating agents such as methyl methanesulfonate (15). Seki *et al.* (13) recently purified human POLQ and examined its catalytic activity. POLQ has extremely low fidelity, making frequent errors on undamaged templates. Moreover, POLQ was shown to be the only enzyme to efficiently catalyze both the insertion and extension steps that allow bypass of abasic sites (16).

The function of Polθ in mammalian cells remains poorly understood. In a phenotype-based mutagenesis screen for chromosome instability mutants, Shima *et al.* (12) identified a mouse mutation called *chaos1* (chromosome aberration occurring spontaneously), which exhibited elevated levels of spontaneous micronuclei in reticulocytes. The *chaos1* mutation introduced a T-to-C base substitution in the *Polq* gene, which caused a serine-to-proline substitution at amino acid residue 1932 in this very large protein. Very recently, these investigators have generated Polθ-deficient mice, which have a phenotype very similar to *chaos1*, thus confirming the identity of *Polq* and *chaos1* (17). Surprisingly, besides increased micronuclei in reticulocytes, the Polθ-deficient mice did not show any obvious phenotype and displayed the same sensitivity as normal mice to the DNA crosslinking agent mitomycin C and to γ-irradiation.

Unlike other low-fidelity DNA polymerases, which are ubiquitously expressed, human and mouse *Polq* exhibit a tissue-specific expression pattern. We found preferential expression in lymphoid tissues; most interestingly, abundant *Polq* transcripts were detected in GC B cells, the target cells for both SHM and CSR (18). The lymphoid tissue-specific expression pattern of *Polq* in both human and mouse suggested that Polθ might have a specialized role in mammalian lymphocytes.

To investigate the polymerase function of Polθ in SHM, here we have generated mice specifically devoid of Polθ polymerase activity (Polq-inactive), leaving helicase and other potentially important functional domains intact. Compared with WT mice, Polq-inactive mice exhibited a moderate decrease in overall mutation frequency in the J_H4 intronic sequence of responding B cells, a genomic region chosen for analysis to avoid antigen-selection bias. Remarkably, however, only mutations at C/G were specifically reduced in Polq-inactive mice, whereas mutations at A/T were not affected. We propose that the polymerase activity of Polθ mediates the generation of C/G mutations by replicating over abasic sites formed by uracil-DNA glycosylase-catalyzed excision of the uracil residues generated by activation-induced cytidine deaminase.

This paper was submitted directly (Track II) to the PNAS office.

Abbreviations: NP, 4-hydroxy-3-nitrophenyl-acetyl; NP-CGG, NP coupled to chicken gammaglobulin; SHM, somatic hypermutation; Polθ/ζ/η/ι/κ, DNA polymerase θ/ζ/η/ι/κ; CSR, class switch recombination; GC, germinal center.

**To whom correspondence should be addressed. E-mail: oh@rcai.riken.jp.

www.pnas.org/cgi/doi/10.1073/pnas.0505636102

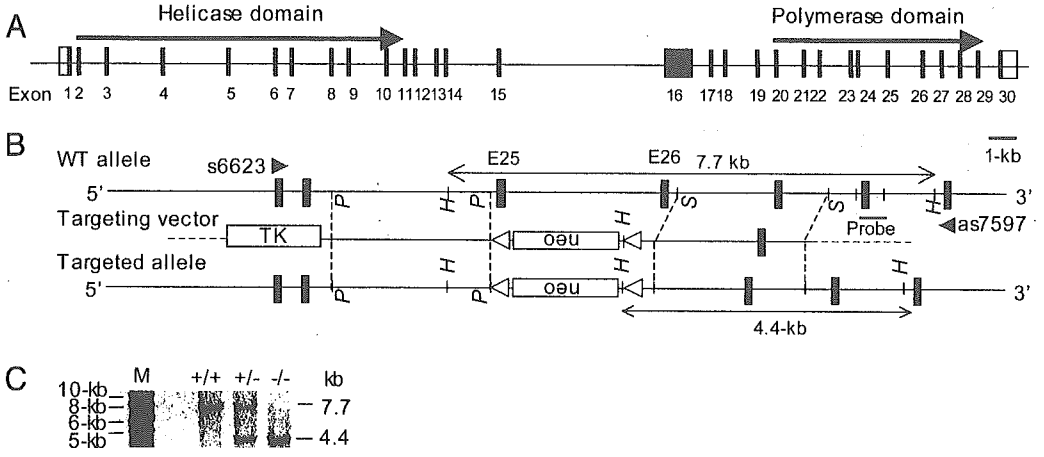

Fig. 1. Disruption of Polθ polymerase core motif. (*A*) Scheme of the mouse *Polq* gene. Solid boxes, exons; open boxes, noncoding regions. (*B*) Targeting strategy. The targeting vector was designed to replace exons 25 and 26 with a neomycin gene. Restriction enzyme sites (P, PvuII; S, SphI; H, HindIII), the probe for Southern blot analysis (solid bar), and PCR primers (s6623 and as7597) are indicated. (C) Southern blot analysis of HindIII-digested ES DNA.

Materials and Methods

Generation of Mice Lacking the Polymerase Core Domain. A targeting vector was constructed to replace exons 25 and 26 with the neomycin gene. R1 ES cells were transfected with the linearized targeting vector and 2 days after transfection cultured in the presence of 600 μg/ml G418 and 2 μM ganciclovir (only for the first 2 days). ES colonies were expanded and subjected to Southern blot analysis to identify homologous recombination. The deletion of exons 25 and 26 was further confirmed by RT-PCR analysis by using primers s6623 (5′-AGCGGGAAAAGCACCTGAAC-3′) and as7597 (5′-CGTCGTGAAGTTGAAGGATG-3′). RT-PCR was performed at 95°C for 2 min followed by 30 cycles of amplification at 95°C for 5 s, 58°C for 10 s, and 72°C for 2 min by using Taq polymerase (Toyobo, Osaka). Chimera mice were bred with C57BL/6N to obtain heterozygous mice. After backcrossing to C57BL/6N for three generations, heterozygous mice were bred with each other to obtain homozygous mice. Mice were kept at specific pathogen-free conditions, and animal experiments were approved by the Animal Facility Committee of the RIKEN Yokohama Institute.

Assay for Polymerase Activity. Polyclonal rabbit antibodies were raised against a peptide (QNDRTGLLPKRKLKG) located near the C terminus of mouse Polθ. For immunoprecipitation, 5×10^7 spleen cells were incubated for 30 min on ice in 0.5 ml of lysis buffer, as described (16) The lysate was centrifuged for 10 min at 15,000 rpm, and the supernatant was precleared four times with 0.5 ml of protein A beads. The precleared lysate was incubated with 10 μl of protein A beads at 4°C for 4 h and washed five times with the lysis buffer. Half of the washed beads were used for the polymerase assay and the remaining half of the beads for Western blot analysis. The polymerase assay was performed essentially as described by using ^{32}P-labeled 16 mer (5′-CACTGACTGTATGATG-3′) annealed to a 30 mer (5′-CTCGTCAGCATCTACATCATACAGTCAGTG-3′) oligonucleotide as a template (16).

Flow Cytometry Analysis and Proliferation Assay. Flow cytometry analysis was performed as described (19). For proliferation assays, B cells were purified by negative selection from spleen of 8- to 12-wk-old mice by using a B cell enrichment set (BD Biosciences, San Jose, CA). Stimulation with anti-IgM antibodies, CD40 ligand, and LPS and ^{3}H-thymidine uptake was essentially as described (20).

Immune Response. Five WT and eight Polq-inactive mice (9–10 wk old) were injected i.p. with 100 μg of 4-hydroxy-3-nitrophenyl-acetyl (NP) coupled to chicken gammaglobulin (NP-CGG) (Biosearch) precipitated with alum and boosted 4 wk later. Mice were bled weekly, and serum titers of NP-specific IgG1 were analyzed by ELISA, by using NP-specific monoclonal high- (clone C6) and low- (clone N1G9) affinity antibodies as a standard (21).

SHM Assay. Five pairs of age- and sex-matched WT and Polq-inactive mice (16 wk old) were immunized with 100 μg of NP-CGG and 2 weeks later, B220$^+$PNA$^+$ GC B cells were sorted. All mice were IgM$^{b/b}$ as determined by FACS analysis of peripheral blood leukocytes by using allotype-specific antibodies (FITC anti-IgM^a and PE-anti-IgM^b, BD Biosciences). Genomic DNA was isolated from sorted GC B cells and amplified with forward primer J558Fr3 (5′-CAGCCTGACATCTGAGGACTCTGC-3′) and reverse primer JHCHint (5′-CTCCACCAGACCTCTCTAGACAGC-3′), as described (22). PCR was carried out with KOD-Plus polymerase (Toyobo) under the following conditions: 94°C for 5 min and then 94°C for 20 s, 65°C for 30 s, and 68°C for 70 s for 30 cycles. The PCR products were cloned into the pCR2.1 vector for sequencing. Only clones with unique V(D)J junctions were analyzed.

Results

Generation of Mice Specifically Devoid of Polθ Polymerase Activity. To specifically inactivate the DNA polymerase activity of Polθ while leaving the helicase and other potentially important domains intact, we deleted exons 25 (185 base pairs) and 26 (112 base pairs), which encode a conserved aspartic acid residue known to be essential for the polymerase catalytic activity (23, 24) and the tyrosine residue that binds the incoming nucleotide (11, 14), respectively (Fig. 1 *A* and *B*). Homologous recombination in ES cells was monitored by Southern blot analysis (Fig. 1*C*). Because the deletion of these two exons was in-frame and the *Polq* promoter was intact, the targeted allele could theoretically be transcribed and translated. As predicted, RT-PCR analysis by using primers flanking exons 25 and 26 (s6623 and as7597, Fig. 1*A*) gave rise to a 975-bp band in WT and a 678-bp band in mutant cells (Fig. 2*A*), although the level of mutant *Polq* was slightly reduced, possibly due to the intronic insertion of the neomycin gene. We further sequenced each of the two bands and confirmed that they were derived from WT mRNA and mRNA lacking exons 25 and 26 (data not shown). Consistent with the